International Journal of Fatigue 144 (2021) 106038

Contents lists available at ScienceDirect

International Journal of Fatigue

journal homepage: www.elsevier.com/locate/ijfatigue

An investigation into the effects of cyclic strain rate on the high cycle and very high cycle fatigue behaviors of wrought and additively manufactured Inconel 718

Muztahid Muhammad [a,b], Palmer Frye [c], Jutima Simsiriwong [b,c,*], Shuai Shao [a,b], Nima Shamsaei [a,b,*]

[a] Department of Mechanical Engineering, Auburn University, Auburn, AL 36849, USA
[b] National Center for Additive Manufacturing Excellence (NCAME), Auburn University, Auburn, AL 36849, USA
[c] School of Engineering, University of North Florida, Jacksonville, FL 32224, USA

ARTICLE INFO

Keywords:
Very high cycle fatigue
Ni-base superalloy
Frequency effects
Anisotropy
Additive manufacturing

ABSTRACT

Additive Manufacturing (AM) has increasingly been used to fabricate parts in aerospace applications, which may require service lives beyond ten-million cycles due to the imposed high loading frequencies. Understanding the very high cycle fatigue (VHCF) behavior of these additive manufactured (AM) parts is an important step towards their design and qualification processes. This study focuses on the high cycle fatigue (HCF) and VHCF behaviors of both wrought and laser beam-powder bed fusion (LB-PBF) fabricated Inconel 718 in machined/polished surface condition, emphasizing on the influence of test frequency (i.e., cyclic strain rate). Uniaxial, fully-reversed force- and stress-controlled fatigue tests were conducted utilizing a servo-hydraulic and an ultrasonic test system operating at 5 Hz and 20 kHz, respectively, on wrought as well as LB-PBF vertically and diagonally built specimens. Fatigue cracks in the majority of the specimens were found to initiate from intra-granular slip bands near or at the surface, which gives rise to strong anisotropy in fatigue resistance in LB-PBF specimens due to the presence of columnar grains along the build directions. Longer fatigue lives were obtained at 20 kHz, which was ascribed to possibly lower-than-intended stresses applied in the ultrasonic tests. The corrected stress-life fatigue data at 20 kHz were found to converge to the one obtained from conventional testing at 5 Hz, implying no effect of cyclic strain rate on the fatigue behavior of Inconel 718 regardless of the fabrication process. The findings of this work confirm the use of ultrasonic fatigue testing to expedite generation of AM materials data to keep up with the current demand; however, the applied stress may need to be corrected.

1. Introduction

Metal additive manufacturing (AM) techniques have recently become of great interest to the aerospace industry, especially for their significant potential to replace conventional manufacturing methods producing gas-turbine engine components [1–4]. Since no special tooling or molds are required to build a part, AM techniques are expected to allow for more complex part geometries and less material waste when compared to the traditional manufacturing techniques. Although the popularity of AM of metals has increased tremendously, the structural integrity of parts produced via AM has yet to be adequately characterized for use in critical aerospace applications [5,6]. Before AM can be used to produce parts for fatigue-critical applications, the mechanical behavior of the material, especially under cyclic loading (i.e., fatigue), must be fully understood.

Ni-base superalloys owe their recognition to a noteworthy combination of exceptional mechanical properties including high strength as well as corrosion and creep-rupture resistance in a wide range of operating temperatures [2,7,8]. Inconel 718 (abbreviated here on after as IN718) is a γ-γ'-γ'' Ni-base superalloy that is commonly used in gas-turbine and rocket engine components, as it can maintain acceptable mechanical properties at temperatures approaching 650 °C which is the decomposition temperature of its primary strengthening phase γ''. In such applications, IN718 parts are often subjected to cyclic loading at very high frequency and service lives that well exceed ten-million cycles

* Corresponding authors at: School of Engineering, University of North Florida, Jacksonville, FL 32224, USA (J. Simsiriwong). Department of Mechanical Engineering, Auburn University, Auburn, AL 36849, USA (N. Shamsei).
E-mail addresses: j.simsiriwong@unf.edu (J. Simsiriwong), shamsaei@auburn.edu (N. Shamsaei).

https://doi.org/10.1016/j.ijfatigue.2020.106038
Received 11 September 2020; Received in revised form 31 October 2020; Accepted 9 November 2020
Available online 23 November 2020

Nomenclatures

$2N_f$	Reversals to failure
a	Crack length
a_{CF}	Crack length in specimen subjected to conventional fatigue testing
a_{UF}	Crack length in specimen subjected to ultrasonic fatigue testing
E^*	Cyclic modulus of elasticity
ε_a	Strain amplitude
$\dot{\varepsilon}$	Strain rate
f	Frequency
K_C	Mode I fracture toughness
R	Stress ratio
σ_a	Stress amplitude
σ_{max}	Maximum stress
σ_{min}	Minimum stress
σ_{UF}^C	Corrected stress amplitude for the specimen in the ultrasonic fatigue machine
σ_{UF}	Input stress amplitude in the software in ultrasonic fatigue machine
J	The rates of events associated with dislocations' motion, including glide and cross-slip
J_0	Rate constant
σ	Activation stress
Ω	Activation volume
ΔG	Activation energy
k	Boltzmann's constant
T	Temperature in Kelvin

Abbreviations

AM	Additive manufacturing/manufactured
APBE	Anti-phase boundary energy
BCC	Body centered cubic
CIS	Crack initiating site
CNC	Computerized numerical control
D	Diagonal, used for specimens fabricated at 45° with respect to build plate
EBSD	Electron back-scatter diffraction
EDS	Energy dispersive spectroscopy
FCC	Face centered cubic
HCF	High cycle fatigue
IN718	Inconel 718
IPF	Inverse polar figure
KAM	Kernel average misorientation
LB-DED	Laser beam-directed energy deposition
LB-PBF	Laser beam-powder bed fusion
LCF	Low cycle fatigue
LEFM	Linear elastic fracture mechanics
LoF	Lack of fusion
MMPDS	Metallic Materials Properties Development and Standardization
PSB	Persistent slip bands
SEM	Scanning electron microscope/microscopy
SFE	Stacking fault energy
V	Vertical, used for specimens fabricated at 90° with respect to the build plate
VHCF	Very high cycle fatigue
XCT	X-ray computed tomography
XRD	X-ray Diffractometer/X-ray diffraction

($>10^7$ cycles); therefore, a thorough understanding of very high cycle fatigue (VHCF) behavior (i.e., cyclic loading beyond 10^7 cycles) of IN718 is critical.

Comprehensive characterizations of the VHCF performance is challenging since a) conventional fatigue tests are typically conducted at 20 Hz or lower and cannot reach the VHCF regime efficiently [4,7], b) although the novel ultrasonic fatigue tests operating at 20 kHz can easily reach 10^9 cycles [4,7,9–11], the imposed significantly higher cyclic strain rates may influence the cyclic stress–strain behavior, and consequently, the measured fatigue strength/life, which may render them inapplicable to service conditions at lower strain rates. This is because slip related events such as cross-slip, as the main mechanisms by which cyclic damage is accumulated, are thermally activated and rate dependent. Under higher strain rates (such as during ultrasonic fatigue), the occurrences of these events may be limited, leading to reduced damage accumulation. The sensitivity of fatigue damage accumulation to the cyclic strain rate, which has been shown to strongly depend on the material, needs to be carefully characterized for IN718 [4,5,12,13].

To date, the limited VHCF studies [7,14–17] on wrought IN718 using ultrasonic loading conditions have revealed that cracks initiate from sub-surface anomalies and weak points in the microstructure, which contrasts with the surface crack initiation typically observed in the HCF regime. The surface-to-internal transition of crack initiation sites (CIS) from HCF to VHCF was believed to originate from the reduction of load amplitude which essentially eliminates the surface dominated, cyclic plasticity [18]. In the VHCF regime, the plasticity is extremely localized and is limited to the vicinity of microstructural related stress risers, such as brittle particles and grain boundaries. The main sources of sub-surface crack initiation for IN718 are brittle metal carbides and coarse grains containing twin boundaries [7]. It has also been proposed that there exists an optimal value for austenite grain size as well as the population of carbides within the matrix to achieve the highest VHCF resistance for wrought IN718 [7].

For AM materials, studies on the VHCF behavior of Ni-base superalloys have been scarce- only one is available to the authors' best knowledge [19]. In [19], the machined, laser beam-powder bed fusion (LB-PBF) fabricated IN718 specimens were shown to have fatigue cracks initiated from process-induced defects, including entrapped gas pores and lack of fusion (LoF) defects, which substantially deteriorated their fatigue performance compared to their wrought counterparts.

To sum, VHCF studies on IN718 are still very limited in the literature regardless of the manufacturing technologies [7,14–17,19]. In addition, most of these studies, although have generated valuable data and important mechanistic understandings on the fatigue failure of IN718 in the VHCF regime, did not directly investigate the effect of frequency (i.e., cyclic strain rate) [14,19]. Although there have been attempts to quantify the frequency effects for wrought IN718 leveraging uniaxial ultrasonic fatigue tests [14,15], comparisons have been made with low-frequency rotation bending [20,21] and push–pull data [22] in the literature. Well-controlled, side-by-side comparison of fatigue data from conventional and ultrasonic tests with similar loading conditions, isolating only the cyclic strain rate effects, is still lacking for both wrought and AM IN718.

On another vein, the fatigue behavior of AM materials, in the HCF regime and under conventional frequencies, can be sensitive to the loading direction with respect to their layer orientation [23–25]. This anisotropy has been commonly ascribed to the presence of orientation dependent defects, such as the LoF defects, which are usually formed perpendicular to the build orientation, and elongated grains that are typically oriented parallel to the build orientation [26]. For instance, due to the alignment of the LoF defects with the maximum shear plane, diagonally-built specimens can exhibit lower fatigue resistance than the vertically built specimens in some AM materials [24,25]. Indeed, it has been seen in wrought materials with artificial defects (surface notches)

subjected to cyclic loading, defects which are aligned to the plane of maximum shear stress, the cracks typically initiate with less number of cycles compared to the defects oriented at 0° or 90° to the plane of maximum shear stress [27].

Hypothetically, even with the absence of LoF defects, the diagonally build specimens may still have lower fatigue resistance, since the elongated grains are aligned with the plane with the maximum shear stress leading to significantly higher slip distances. Although the orientation effect is known in the low cycle fatigue (LCF) and HCF regimes [28], this effect is hitherto unexplored in the VHCF regime.

The main objective of the present study is therefore two-fold:

1) To quantify the effect of load frequency (therefore the cyclic strain rate) on the uniaxial fatigue behavior of both wrought and LB-PBF IN718;
2) To quantify the effect of build orientation on uniaxial fatigue behavior of LB-PBF IN718 in the VHCF regime.

In the present study, the conventional fatigue testing technique using a servo-hydraulic system and an ultrasonic fatigue system were employed probe into both HCF and VHCF regimes. To the best knowledge of the authors, the present study offers the first data set on the effect of cyclic strain rate on the fatigue performance of both wrought and LB-PBF IN718. The research performed in this study will also help with determining whether or not ultrasonic fatigue testing at very high frequency can be used to generate fatigue properties for AM materials to expedite their qualification process. The findings of this work suggested that the equivalency of fatigue tests for both conventional and ultrasonic frequencies to be carefully established before ultrasonic tests can be adapted to rapidly generate fatigue data of AM materials.

Machined specimens made from both wrought and LB-PBF IN718 in the vertical and diagonal orientations were tested. The geometries of the test specimens for both testing frequencies were designed to be as close as possible, within the constraint of standards and equipment manufacturer recommendations, to achieve a near-identical state of stress at the gage sections. Fatigue lives of machined specimens from 10^3 to 10^7 reversals were measured in the conventional fatigue tests and lives from 2×10^4 to 2×10^9 reversals were measured in the ultrasonic fatigue tests, permitting cross referencing of data over a broad life regime and reliable quantification of cyclic strain rate effects.

This article is organized as the following: In Section 2, experimental procedures including the description of material and specimen fabrication, porosity analysis, microstructure and fractography analysis, as well as the description of conventional and ultrasonic fatigue testing is provided. In Section 3, experimental results were summarized which include porosity analysis, characterization of microstructure, uniaxial fatigue behavior under both conventional and ultrasonic tests, and analysis of fracture surfaces. Section 4 is devoted to discuss and rationalize the key experimental findings, followed by summarizing the findings and stating concluding remarks in Section 5.

2. Experimental procedures

2.1. Material and specimen fabrication

Test specimens were fabricated using an LB-PBF process via the EOS M290 additive manufacturing system in an argon purged environment. Suggested process parameters provided by the manufacturer for the EOS M290 system (see Table 1) were utilized for all AM part fabrications in this study. Oversized LB-PBF specimens were fabricated in two build directions, vertical (V) and diagonal (i.e., bar axis 45° with respect to the build plate, D) using the oversized dimensions and geometries shown in Fig. 1 (a) and 1 (b) for conventional and ultrasonic fatigue tests, respectively. After fabrication, all specimens were subjected to heat treatment according to SAE AMS2774E [29] for nickel alloy parts. Following this procedure, specimens were first held at a minimum of 10 min at a solution set temperature of 954 °C. They were subsequently transferred to a separate furnace and held at 718 °C furnace for 8 h, and 621 °C for an additional 10 h.

Table 1
Manufacturer suggested LB-PBF process parameters for IN718 by EOS M290.

Laser power	285 W
Scanning speed	960 mm/s
Hatching space	110 μm
Layer thickness	40 μm
Shielding gas type	Argon

After heat treatment, the oversized specimens were then machined using a computer numerical control (CNC) lathe to the final dimensions shown in Fig. 1 (c) and 1 (d) for conventional and ultrasonic fatigue testing, respectively. The dimensions and geometries of the ultrasonic specimens in Fig. 1 (d) were established based on the recommendation by the ultrasonic fatigue test system manufacturer, Shimadzu Scientific [30], to achieve the required natural frequency. The dimensions of the hour-glass specimens for conventional fatigue tests follow the ASTM E466 standard [31], and to minimize stress concentration in the gage section, the radius of the diameter of the hour-glass gage was>8 times than the minimum diameter of the gage section for both conventional and ultrasonic testing to meet the standard requirement. However, the minimum diameter and volume at the gage section more closely follow the dimensions of specimens used for ultrasonic fatigue testing to ensure consistency in the state of stress in both types of specimens.

In addition, wrought specimens for both conventional and ultrasonic fatigue testing were fabricated from 15.9 mm round bar stocks and machined using a CNC lathe. As-received (purchased from “Online Metal Supply” [31]) wrought IN718 bars had been processed and heat-treated according to the SAE AMS2774E standard; therefore, no additional heat treatments were applied to wrought IN718 specimens. Following machining, all specimens, including wrought and LB-PBF ones, were polished using 400 grit, 800 grit, 1000 grit, 1500 grit, and 2000 grit silicon carbide cloths, respectively, to remove machining marks from their gage sections.

2.2. Porosity analysis

A ZEISS Xradia 620 Versa X-ray computed tomography (XCT) machine was used to analyze the porosity of a typical specimen for conventional frequency testing (as shown in Fig. 2 (a)) at the gage section. A total volume of 25.9 mm^3 in the specimen gage section was scanned. ImageJ software was used to analyze the pores from the images of the XCT scan. The result of the XCT-based porosity analysis was cross-checked with the polished cross-section optical analysis using a Keyence microscope. For the optical analysis, the specimen gage was sectioned 5 times on the radial direction (normal to the build direction) and polished before imaging, and an average porosity reading was calculated.

2.3. Microstructure and fractography analyses

Initial microstructural analysis was performed using a Tescan Mira3 field emission scanning electron microscope (SEM). Wrought and LB-PBF IN718 grain characteristics were investigated by electron backscatter diffraction (EBSD) measurements using an Oxford system. Secondary phases and precipitates were identified through energy dispersive spectroscopy (EDS) analysis on metallographic samples. Metallographic samples were sectioned using a slow speed saw and experienced preliminary grinding and polishing with 120 grit, 240 grit, 400 grit, 600 grit, 1200 grit grinding discs, and 6 μm and 1 μm lapping films with polishing pads. To ensure the consistent surface quality in all specimens, a final vibratory polishing was performed using a 0.02 μm lapping film for 12 h. High-resolution fracture surface imaging was

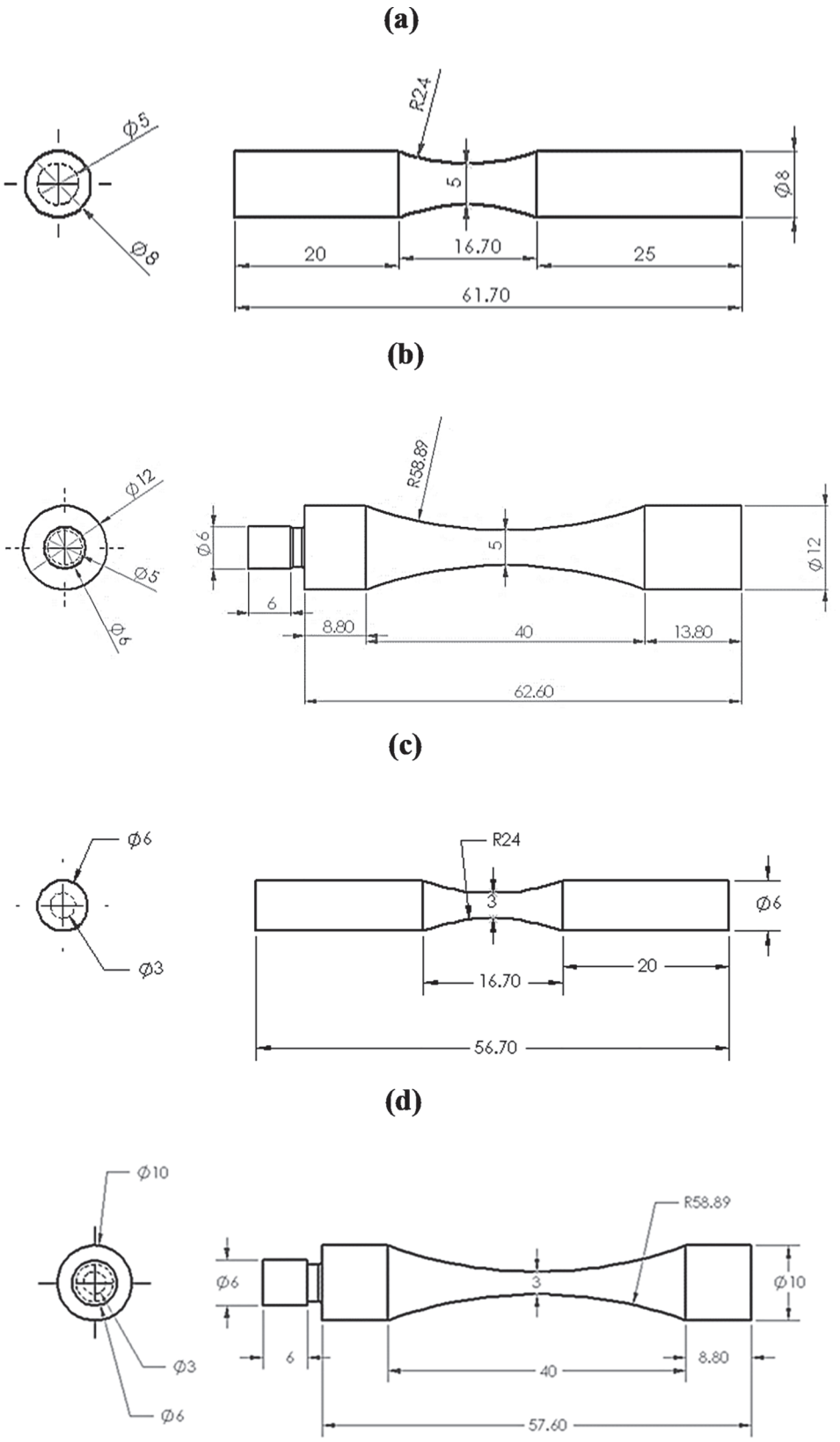

Fig. 1. Geometries and dimensions for oversized IN718 specimens for (a) conventional and (b) ultrasonic fatigue tests. These oversized specimens were machined to the final geometries and dimensions shown in (c) for conventional and (d) for ultrasonic fatigue testing.

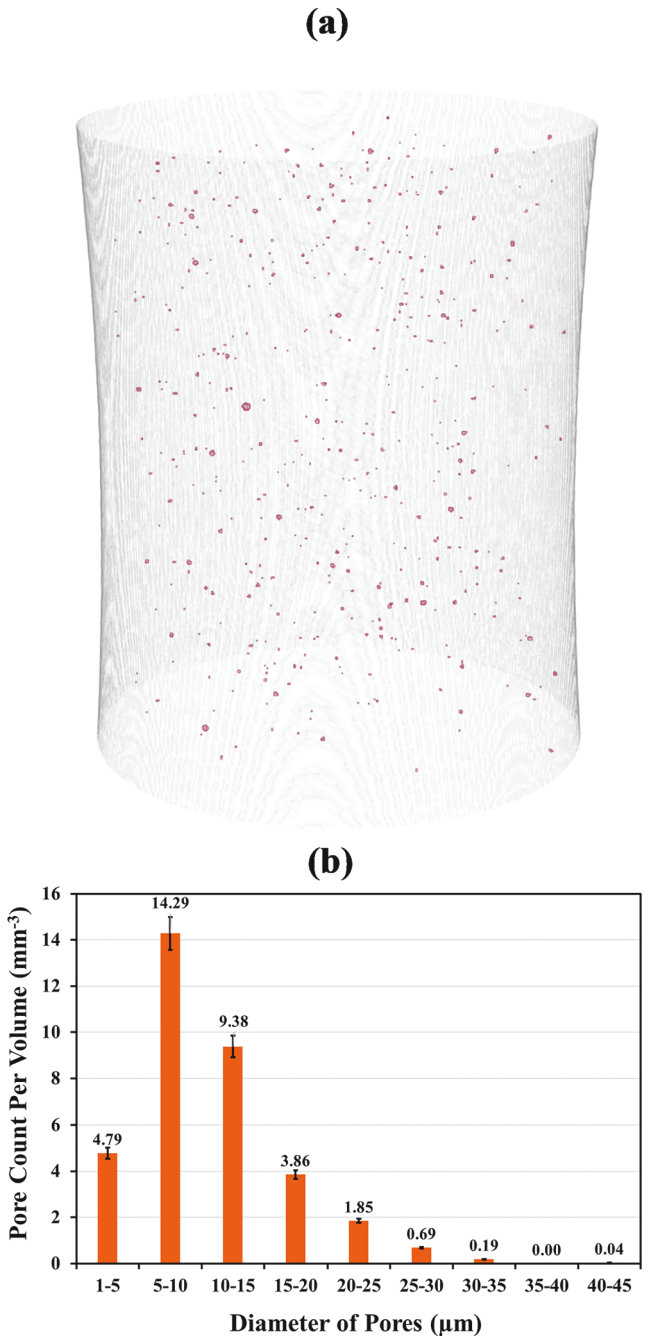

Fig. 2. (a) X-ray CT scanned section of a machined vertical LB-PBF IN718 specimen for porosity analysis, and (b) porosity size distribution of the specimen.

performed using the Tescan Mira3 field emission SEM and the Zeiss Crossbeam FIB-SEM to identify crack nucleation, fatigue striations, and crack propagation regions.

2.4. Micro-hardness testing

To qualitatively compare the strengths of the wrought and the heat treated LB-PBF IN718, an Anton Paar Nanoindentation Hardness Tester (NHT2) (Anton Paar GmbH) was used. Prior micro-hardness testing, both wrought and LB-PBF IN718 samples were mounted and polished until mirror finish. For micro-hardness testing, a Vicker's indenter was employed along with a load of 100 mN and a loading rate of 2000 mN/min with 0 s hold time. To confirm the measured value, micro-hardness readings were repeated at 10 points for each sample.

2.5. Conventional fatigue testing

Fully-reversed ($R = \sigma_{min}/\sigma_{max} = -1$) force-controlled uniaxial fatigue testing was conducted using MTS servo-hydraulic test system with a 100 kN load cell. Tests were performed according to the ASTM E466 standard [31] at room temperature and room relative humidity. Cyclic loading was applied using a sinusoidal waveform and a test frequency of 5 Hz for all tests. At least two fatigue tests were performed at each force level. Specimens with a life exceeding 2×10^7 reversals were considered as runout tests.

2.6. Ultrasonic fatigue testing

Ultrasonic fatigue testing in this study was conducted under fully-reversed loading at 20 kHz at room temperature and room relative humidity, employing a Shimadzu USF-2000A ultrasonic fatigue test system. A piezo actuator oscillates at a frequency of 20 kHz, which achieves a stationary longitudinal waveform through the amplify horn and test specimen, thus allowing the test specimen to resonate. The dimensions and geometry of the specimen are designed so that the maximum stress is applied to the gage section only, and the maximum displacement occurs at the free end and the clamped end of the specimen.

During testing, the specimen temperature was closely monitored using a laser thermometer. The temperature rise of the specimen was kept less than 30 °C to minimize any temperature effects on the results. Temperature rise was also minimized using compressed air flow directly to the gage section of the specimen, as well as intermittent driving pulse/pause conditions to negate thermal expansion effects from self-heating. Intermittent pulse/pause parameters varied from 110/800 msec to 110/4000 msec, depending on the stress amplitude. Calibrations of extensometer and piezo-electric transducer were carried out prior to testing. In contrast to the conventional fatigue tests, no tests were run to fracture. Instead, each test was terminated when the observed change in the resonance frequency of the test sample exceeded 500 Hz. The runout for the ultrasonic fatigue testing was set to 2×10^9 reversals. The failed specimens were then pulled apart using a tensile machine to expose the fracture surfaces.

3. Experimental results

3.1. Porosity analysis

Fig. 2 (a) shows a qualitative three-dimensional representation of volumetric defects in the hour-glass gage section of the V LB-PBF specimen fabricated for conventional fatigue testing. All the defects have been identified as gas-entrapped pores. Fig. 2 (b) exhibits the pore size distribution in the gage section over a volume of 25.9 mm^3 measured during the XCT scan. A total of 909 pores were identified in the scanned region, with pore diameters ranging from 4.64 µm to 41.19 µm. The majority of pores were below 15 µm diameter. On average, around 35 pores were observed per mm^3 volume. These findings from XCT were found to be consistent with the observations from the optical analysis on several polished cross-sections.

3.2. Microstructural observations

Typical microstructures of wrought and LB-PBF IN718 heat treated to the same SAE AMS2774E specifications are displayed in Fig. 3. An equiaxed microstructure is evident for wrought IN718 (Fig. 3 (a)), while columnar grains along the build direction are clearly visible for LB-PBF IN718 (Fig. 3 (b)). Although IN718 is a γ-γ'-γ'' (major phases) alloy, under low magnifications (Fig. 3 (a)), only the (face centered cubic (FCC)) γ grains are visible in the wrought microstructure. In addition, some bright contrast decorating the grain boundaries and, in rare cases,

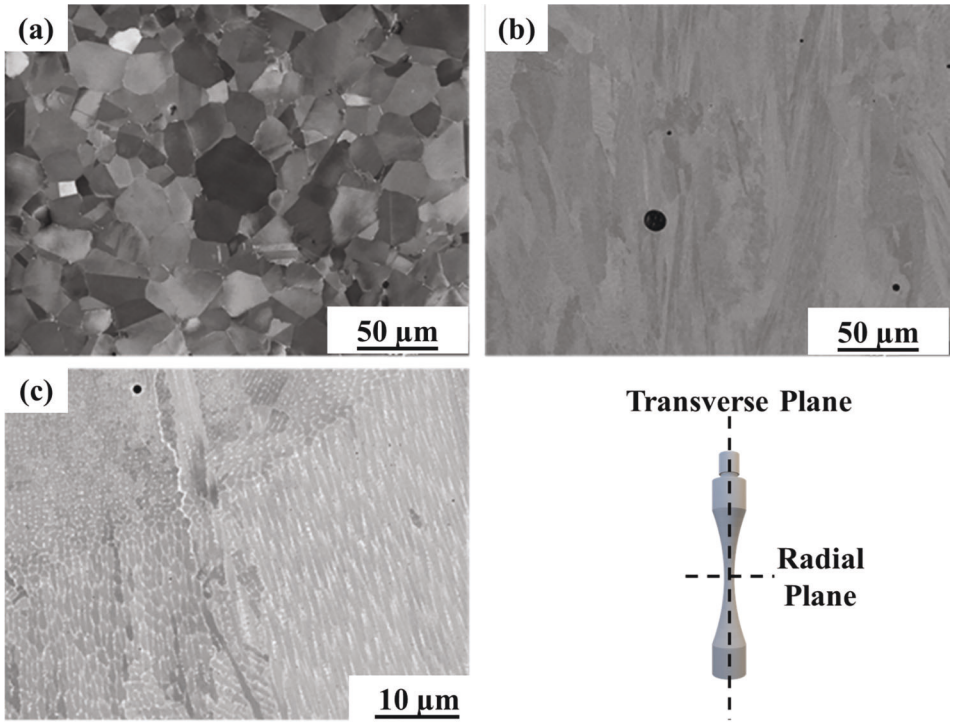

Fig. 3. Microstructures of (a) wrought IN718 with equiaxed grains and (b) post process heat treated LB-PBF IN718 with columnar grains and the remnant of dendritic structures, both imaged in the transverse plane. LB-PBF IN718 shows (c) sub-grain structures with Nb rich boundaries.

the grain interiors are also visible in Fig. 3 (a). The platelets may be δ precipitates with chemical formula of Ni_3Nb, while the small bright gobbles may be metal carbides [32]. Conventionally-processed IN718 can also contain trace amounts of an additional secondary phase known as Laves phases (chemical formula $(Ni,Fe,Cr)_2(Nb,Mo,Ti)$); however, based on the morphology of the precipitates observed in the micrographs shown in Fig. 3 (a), its presence in the microstructure is inconclusive.

In this study, the heat treated LB-PBF IN718 specimens contained sub-granular structures with Nb rich boundaries, which are remnants of the as-fabricated dendritic microstructure [19], and are shown in Fig. 3 (b) in lower magnification and Fig. 3 (c) in higher magnification. Directly aged LB-PBF IN718 is shown to contain Nb rich inter-dendritic boundaries decorated by Laves phases [33,34]. Considering the short solutionizing time specified by SAE AMS2774E, it is expected that the Laves phases also exits in the LB-PBF specimens analyzed in this study. Comparing Fig. 3 (a) and 3 (c), it is evident that the LB-PBF material has less grain boundary precipitation (which could be δ and metal carbides along grain boundaries) compared to wrought IN718.

A typical microstructure, represented by inverse pole figure (IPF) maps, in the transverse and radial planes of wrought, and both V and D specimens obtained via EBSD analysis is shown in Fig. 4. For both V and D specimens, most of the grains shown in Fig. 4, are columnar and elongated in the direction perpendicular to the build plate (i.e., parallel to the build direction). The longitudinal IPF maps of specimens of both build orientations reveal a large scatter in crystallographic orientations, where neighboring grains are separated by high angle grain boundaries.

It is also notable from Fig. 4(b)-4(e) that slight misorientations exist within the large grains of the LB-PBF IN718, which are quantified by kernel average misorientation (KAM) maps for both V and D LB-PBF IN718 in both radial and transverse planes (see Fig. 5). The grain boundaries are shown in green lines. As shown in Fig. 5, these misorientations manifest as low angle sub-grain boundaries are qualitatively similar for LB-PBF IN718 samples fabricated under both build orientations. As a result, the motion of dislocations may be limited by these boundaries leading to moderate strengthening. Nevertheless, as the resistance of these boundaries to dislocations' gliding is less than that of the high-angle grain boundaries, the slip distances within the grains are still dictated by the high-angle grain boundaries.

The average grain size observed from the radial plane IPF maps in Fig. 4 (c) and 4 (e) is ~11.4 µm for the V specimen and ~12.7 µm for the D specimen. The LB-PBF microstructures comprise very large grains (diameter > 100 µm) decorated by very small grains (5 ~ 10 µm) in the interior of (or at the boundaries between) the large grains. For the wrought material used in this study (shown in Fig. 4 (a)), the average grain size is ~19 µm. The grain size is much more uniform. Therefore, although the average grain size of the wrought specimens is slightly larger, the LB-PBF should still permit longer slip distances under deformation. The grain size distribution in grain counts per area as well as area-weighted fraction histograms for the LB-PBF and wrought specimens are provided in the histograms in Fig. 6. The grain counts are based on scanning of 400 µm × 400 µm area for V and D LB-PBF in the radial plane and 350 µm × 400 µm area for wrought IN718 specimens. The threshold misorientation angle for grain boundary detection was 10°, and border grains (i.e., the grains along the edges of IPF maps) are included while analyzing the grain size distribution. Note that the grains along the edges of IPF maps were not complete.

3.3. *Stress-life fatigue data*

Stress-life fatigue data for wrought as well as V and D LB-PBF IN718 under both testing conditions are listed in Tables 2 and 3. It is notable that, one of the wrought and one of the V specimens tested under conventional frequency at 500 MPa stress amplitude broke at the grip while testing. These data points are mentioned as "*broke at grip*" in Table 2 and marked with arrows in Figs. 7 and 8, presenting the fatigue data graphically. As can be noticed in these figures, the fatigue resistance of specimens, regardless of fabrication conditions, appears to be higher under ultrasonic testing. Although this "improvement" effect is less apparent for D LB-PBF specimens at higher stress amplitudes (see Fig. 7 (c)), a rather consistent factor of ~10 increase in fatigue life is evident for V LB-PBF as well as the wrought ones when ultrasonic fatigue results

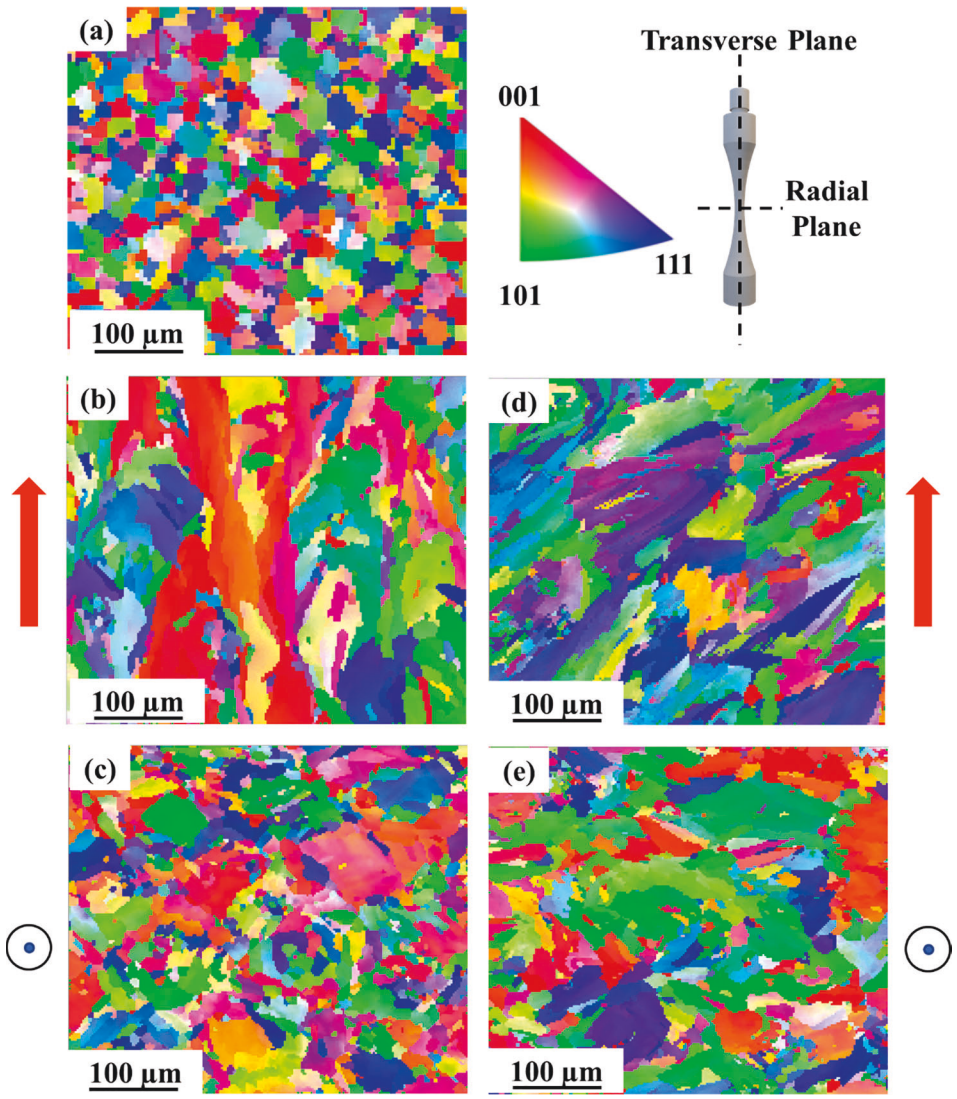

Fig. 4. EBSD obtained IPF-Z microstructures of (a) wrought IN718, vertical LB-PBF IN718 in (b) transverse and (c) radial planes, and (d) transverse and (e) radial planes of a diagonal LB-PBF IN718 specimen. The '*arrows*' (parallel to build direction) and '*circles with a dot*' (coming out of plane i.e., perpendicular to build direction) represent the build orientation of the respective images.

(i.e., 20 kHz) are compared with the conventional ones (i.e., 5 Hz). For comparison, fatigue data of wrought IN718 in unnotched condition collected from Metallic Materials Properties Development and Standardization (MMPDS) [35] is also plotted in Fig. 7 (a). Note that the frequency and the surface finish of the MMPDS stress-life data of IN718 included here were not specified. It is evident that the fatigue data collected from MMPDS is consistent with that of the wrought specimens tested under conventional frequency.

The same stress-life data, now rearranged to illustrate the effect of fabrication conditions, is presented again in Fig. 8, where similar trends can be observed under both test frequencies. Specifically, the V LB-PBF specimens appear to have much better fatigue resistance compared to D LB-PBF specimens in lower stress amplitudes regardless of the test type/frequency. This advantage of the V LB-PBF specimens, however, appears to vanish in the higher stress magnitudes under conventional test frequency (see Fig. 8 (a)). Under ultrasonic frequency, this advantage is also noticeably attenuated in the higher stress levels (see Fig. 8 (b)). It is also quite notable that, under conventional test frequency (i.e., 5 Hz), the V LB-PBF specimens exhibited significantly higher fatigue resistance in all stress levels (2 order of magnitudes better at 700 MPa level and 1 order of magnitude better at 500 MPa) compared to wrought specimens. Under ultrasonic frequency, the V LB-PBF specimens exhibited significantly better fatigue performance than the D LB-PBF ones in all stress levels (2 orders of magnitude better at 500 MPa and 1 order of magnitude better at 700 MPa). However, although the V-LBF specimens showed better fatigue resistance than wrought specimens at high stress amplitudes (1 order of magnitude better at 700 MPa), the difference in fatigue resistance between V LB-PBF and wrought specimens appear to vanish at lower stress levels, such as 500 MPa.

3.4. *Fracture surfaces*

The typical fracture surfaces of the wrought, V LB-PBF, and D LB-PBF specimens are shown in Figs. 9, 10, and 11, respectively. The CISs have been identified on each surface and presented as magnified views in the respective figure. It appears that for wrought IN718 subjected to both conventional and ultrasonic fatigue testing, fatigue cracks have initiated from sub-surface or near surface second phase particles (as pointed to by red arrows in Fig. 8 in the magnified views). This has been confirmed by the EDS analyses on the fracture surfaces. Although the presence of Laves phases was not conclusive from the microstructural observations shown in Fig. 3 (a), EDS analysis confirmed that these particles are rich in Nb, Mo, and Ti, which indicates that they may be Laves phases. In addition, carbides are also often found in close proximities to these CISs.

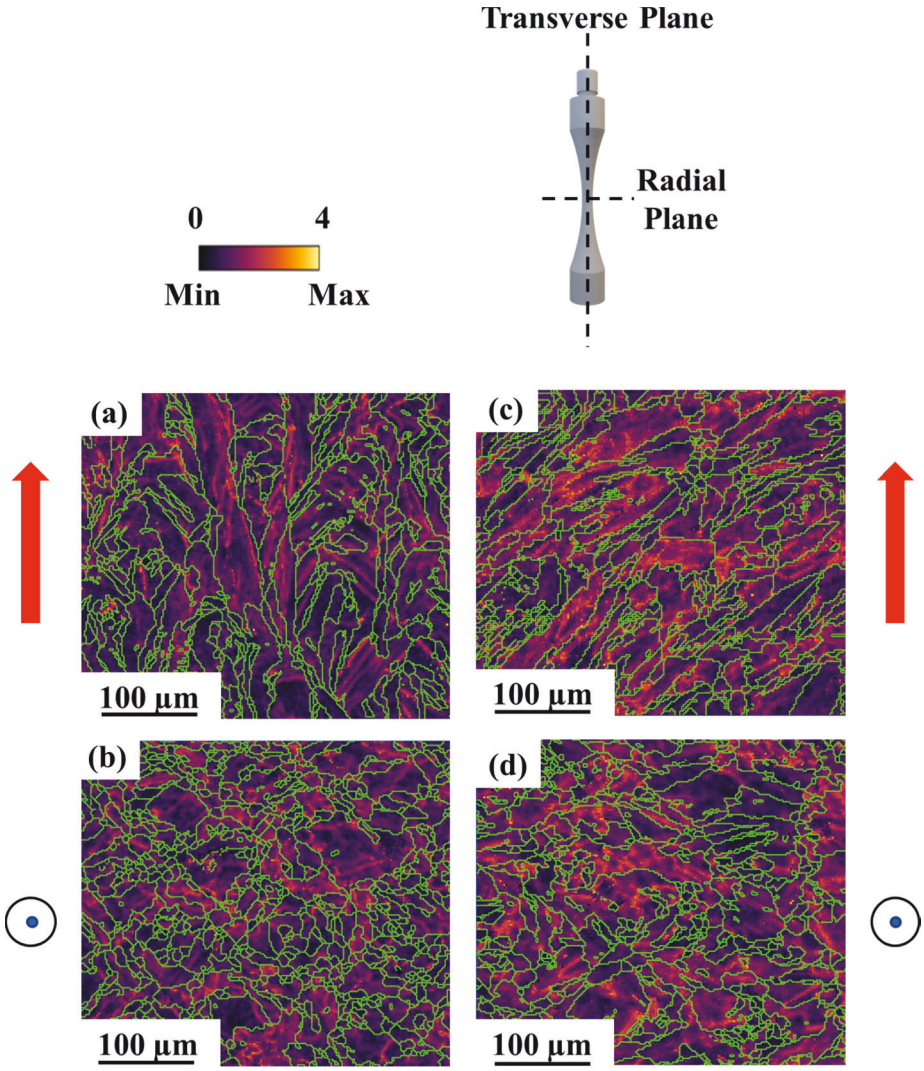

Fig. 5. EBSD obtained kernel average misorientation map of vertical LB-PBF IN718 in (a) transverse and (b) radial planes, and (c) transverse and (d) radial planes of a diagonal LB-PBF IN718 specimen. The '*arrows*' (parallel to build direction) and '*circles with a dot*' (coming out of plane i.e., perpendicular to build direction) represent the build orientation of the respective images. Note that, the grain boundaries are shown by the green lines. (For interpretation of the references to colour in this figure legend, the reader is referred to the web version of this article.)

For both LB-PBF V and D specimens, multiple crystallographic facets are always evident in the areas near the CISs, which indicates the crack initiation due to persistent slip bands (PSB) [36]. The region containing multiple adjoining crystallographic facets can form during the initiation and growth of the microstructurally small crack [37]. The size of these facets is approximately equivalent to that of the width of the columnar grains, which confirms the prior speculation that the high-angle grain boundaries, instead of the low-angle ones, dictate the slip distances. Some obvious and large facets are identified and marked by red dashed enclosures in the magnified views in Figs. 10 and 11. It is assumed that these large facets are the evidence of the large PSB and dominate the initiation of the fatigue cracks. Therefore, they have been registered as the CIS in each fracture surface. Comparing the enclosed areas by red dashed lines in Figs. 10 and 11, it is also notable that the D specimens have larger CISs compared to V specimens, regardless of the testing method (almost ~28% higher in conventional and ~40% in ultrasonic tests). Two possible exceptions in the crack initiation behavior are shown in the magnified views of Figs. 10 (d) and 11 (d), respectively, revealing possible involvement of porosity in rare cases for ultrasonic test method.

It is also noticeable that ultrasonic specimens contain larger crack propagation area compared to their conventional counterparts. This can be clearly seen by comparing the sub-figures (a) and (c) with sub-figures (b) and (d) in Figs. 9, 10, and 11. The crack propagation areas are characterized by relatively flat or faceted regions lined with river marks that can be traced back to the CISs. This observation is quite interesting knowing that the fracture toughness typically decreases by an increase in strain rate, and therefore, the cracks are expected to grow further before final fracture occurs in lower strain rate tests [38,39].

4. Discussion on experimental observations

Three major observations on the fatigue behaviors (summarized below as F1-F3) of wrought and LB-PBF specimens tested under two frequencies were made in Section 3. On the other hand, five major observations were made on the microscopic characteristics (summarized below as M1-M5) of the defect-/micro- structures as well as the fracture surfaces of the specimens. In this section, the observed fatigue behavior (F1-F3) of the wrought and LB-PBF specimens are analyzed and rationalized using their respective microscopic characteristics of microstructure, defects, and fracture surfaces (M1-M5).

Fatigue behaviors:

F1. IN718, regardless of their processing routes, appears more fatigue resistant (by a factor of ~10) under ultrasonic tests (i.e., 20 kHz) compared to when it is conventionally tested (i.e., 5 Hz).

F2. Overall, the LB-PBF specimens appear to have a higher fatigue resistance than wrought at higher stress amplitudes under both loading frequencies, which attenuates at lower stress amplitudes. Similarly, the V LB-PBF specimens appear to be more fatigue

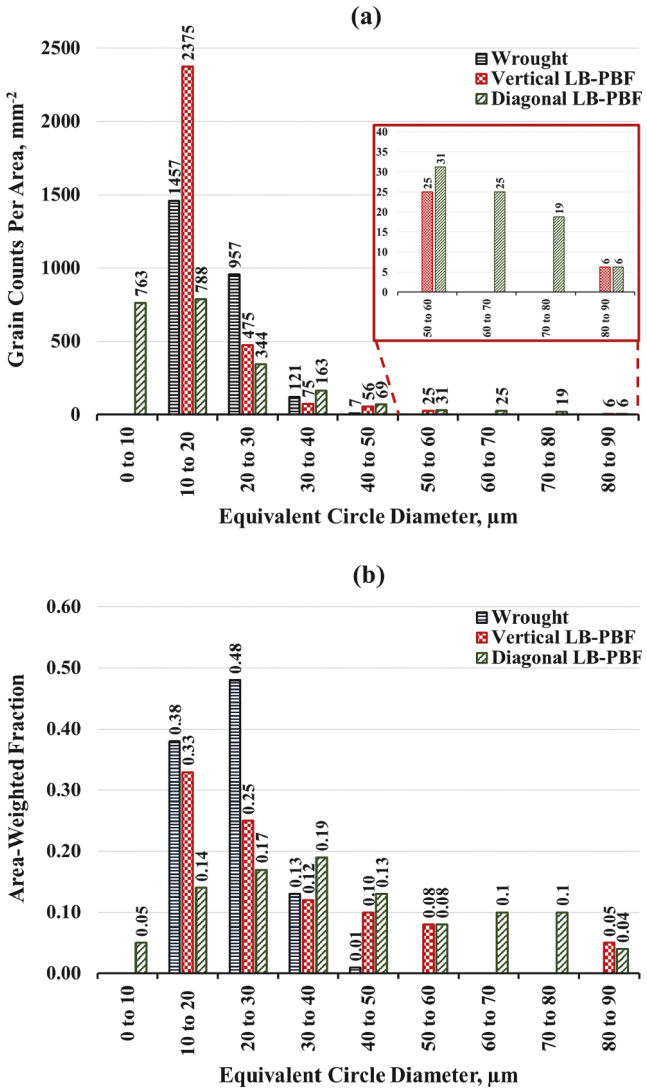

Fig. 6. Histograms depicting grain size distribution in (a) Grain counts per area and (b) Area-weighted fraction for wrought, vertical LB-PBF, and diagonal LB-PBF IN718. The grain size distribution of LB-PBF IN718 is shown in the radial plane.

resistant than the D LB-PBF ones, especially under lower stress levels.

F3. Fatigue cracks predominantly initiated from PSBs near or at surface, barring only two possible involvements of volumetric defects (one V LB-PBF and one D LB-PBF ultrasonic specimens), in contrary to the reports by others [19,40].

Microscopic characteristics:

M1. In LB-PBF specimens, the volumetric defect type is porosity the peak size between 5 and 15 µm. The probability of a large defect (i.e., diameter > 40 µm) residing on the maximum-stress cross-section of the specimens is relatively low, considering the hour-glass shape specimens used in this study.

M2. The microstructure of LB-PBF specimens comprises large columnar grains (diameter > 70 µm at radial cross-sections). Thus, the pores can reside well within these grains.

M3. The as-solidified dendritic microstructure is evident within the columnar grains in the heat treated LB-PBF specimens.

M4. In wrought IN718, cracks initiated mostly from second phase particles likes Laves phases and carbides. However, for LB-PBF IN718, cracks initiated from PSB and there was substantial difference between crack initiating facet sizes between V LB-PBF and D LB-PBF specimens. The average maximum facet length for D LB-PBF specimens is ~ 28% and ~ 40% larger than V LB-PBF specimens in conventional and ultrasonic specimens, respectively.

M5. The conventionally tested specimens for both wrought and LB-PBF IN718 revealed smaller areas for crack propagation on the fracture surfaces than their ultrasonically tested counterparts under the same stress amplitudes.

Table 2
Fatigue test results of IN718 subjected to ultrasonic fatigue testing at 20 kHz.

Specimen type	Specimen ID	Stress amplitude, σ_a (MPa)	Reversals to failure, $2N_f$
Wrought	INW_11	475	6.70E + 07
	INW_12	475	>2.03E + 09
	INW_13	475	4.80E + 08
	INW_7	500	2.00E + 07
	INW_8	500	3.53E + 07
	INW_16	500	>2.00E + 09
	INW_5	525	9.16E + 06
	INW_6	525	2.34E + 07
	INW_15	525	1.37E + 08
	INW_3	550	1.80E + 06
	INW_4	550	9.99E + 05
	INW_14	550	5.93E + 07
	INW_9	575	5.98E + 05
	INW_10	575	3.12E + 06
	INW_1	600	3.96E + 05
	INW_2	600	9.27E + 05
	INW_19	700	1.26E + 05
	INW_20	700	2.70E + 05
	INW_17	800	1.26E + 05
	INW_18	800	1.78E + 04
Vertical LB-PBF	AM_V_1	250	>2.00E + 09
	AM_V_5	350	>2.00E + 09
	AM_V_9	400	>2.00E + 09
	AM_V_2	500	1.04E + 08
	AM_V_3	500	1.07E + 08
	AM_V_6	600	8.31E + 06
	AM_V_4	600	2.20E + 07
	AM_V_7	700	2.79E + 06
	AM_V_8	700	3.36E + 06
	AM_V_10	800	3.90E + 05
	AM_V_11	800	8.91E + 05
Diagonal LB-PBF	AM_D_13	300	3.46E + 08
	AM_D_5	350	6.46E + 07
	AM_D_6	350	1.19E + 08
	AM_D_11	400	4.41E + 07
	AM_D_14	400	4.35E + 07
	AM_D_1	500	4.21E + 06
	AM_D_2	500	7.77E + 06
	AM_D_3	600	1.13E + 06
	AM_D_4	600	1.65E + 06
	AM_D_10	700	7.37E + 05
	AM_D_9	700	6.76E + 05
	AM_D_8	800	1.96E + 05
	AM_D_7	800	1.96E + 05

4.1. Test frequency effects (i.e., cyclic strain rate) on fatigue behavior

IN718 typically nucleate fatigue cracks from slip localization [41] and, in some circumstances, due to the cracking of hard particles such as carbides or Laves phases [42]. Dislocation's motion, as well as the associated interruptive events such as cross-slip, are thermally activated phenomena [43]. The rate of these events (J) obey the Arrhenius law, expressed as [44,45]:

$$J = J_0 \exp \frac{\sigma\Omega - \Delta G}{kT} \quad (1)$$

Table 3
Fatigue test results of IN718 subjected to uniaxial fully-reversed force-controlled testing at 5 Hz.

Specimen type	Specimen ID	Stress amplitude, σ_a (MPa)	Reversals to failure, $2N_f$
Wrought	W_10	475	2.12E + 06
	W_12	475	6.06E + 05
	W_02	500	>6.03E + 06 (*broke at grip*)
	W_09	500	4.61E + 05
	W_04	525	3.38E + 05
	W_01	550	5.47E + 05
	W_08	550	1.50E + 05
	W_03	600	7.71E + 04
	W_07	600	3.58E + 04
	W_05	700	3.73E + 03
	W_06	700	4.84E + 03
	W_11	800	8.82E + 02
Vertical LB-PBF	AM_04	500	>1.02E + 07
	AM_05	500	>6.13E + 06 (*broke at grip*)
	AM_15	600	7.53E + 05
	AM_10	600	1.01E + 06
	AM_21	700	2.41E + 05
	AM_03	700	2.52E + 05
	AM_27	800	8.59E + 04
	AM_25	800	8.27E + 04
Diagonal LB-PBF	MD_03	300	>1.00E + 07
	MD_04	300	>1.00E + 07
	MD_05	400	>1.07E + 07
	MD_10	400	4.93E + 06
	MD_11	400	1.37E + 06
	MD_02	500	8.26E + 05
	MD_06	500	6.66E + 05
	MD_01	600	6.40E + 05
	MD_07	600	5.03E + 05
	MD_08	700	3.90E + 05
	MD_09	700	3.88E + 05

where J_0 is a rate constant, σ and Ω are the activation stress and activation volume, respectively, ΔG is the activation energy, k is the Boltzmann's constant, and T is temperature in Kelvin [46,47]. It stipulates that the rate at which dislocations move/cross-slip is restricted at a given stress and temperature, and implies that at higher cyclic strain rates less cross-slip events occur per cycle because of time restrictions. Accordingly, lack of dislocation motion/cross-slip results in elasticity governing a larger portion of the overall deformation, which ultimately leads in less cyclic damage. Therefore, the damage incurred per cycle under higher cyclic strain rates can be less than that the one under lower strain rates, which may explain why for certain materials the fatigue resistance measured under ultrasonic frequencies is higher than under conventional frequencies.

Fatigue tests conducted in this study were all force-controlled using a constant frequency of 5 Hz for conventional and 20 kHz for ultrasonic tests; therefore, these tests were not conducted using constant strain rates. However, since the stress amplitudes utilized in the study are within the elastic limit of the material, the strain rates can be approximated based on elastic deformation assumption. The average strain rate for conventional and ultrasonic tests are estimated to be ~0.07 s^{-1} and ~200 s^{-1}, respectively, according to the following equation:

$$\dot{\varepsilon} = 4\frac{\sigma_a}{E'}f \tag{2}$$

where $\dot{\varepsilon}$ is strain rate, σ_a is the stress amplitude, f is the test frequency and E' is the cyclic elastic modulus.

It is, however, important to note that the sensitivity of fatigue resistance to cyclic strain rate is material dependent. For instance, the activation volume Ω of dislocation glide in body centered cubic (BCC) metals is significantly smaller than in FCC ones, leading to higher rate sensitivity for BCC [13,48–50]. Similarly, the activation volume for dislocation glide of FCC metals depends on the stacking fault energy

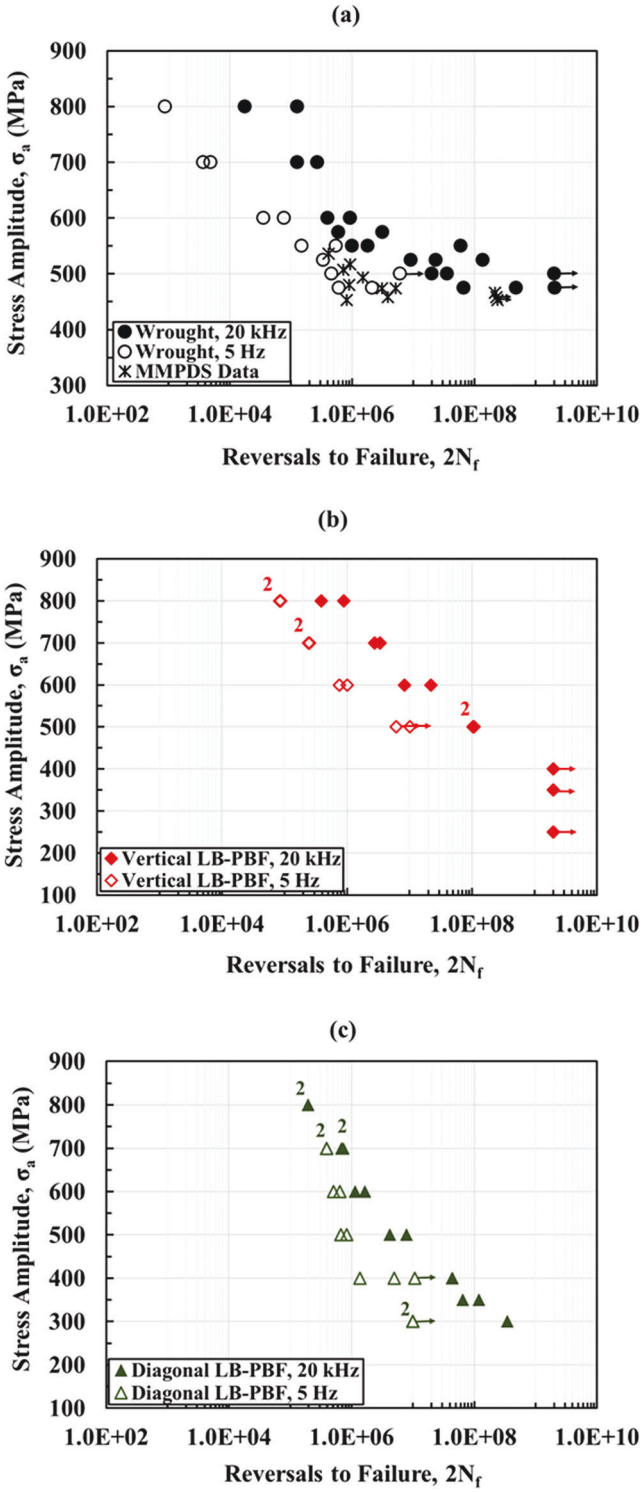

Fig. 7. Stress-life plot for (a) wrought IN718, (b) vertical LB-PBF IN718, and (c) diagonal LB-PBF IN718 tested using conventional and ultrasonic fatigue test methods. In (a), wrought IN718 data from MMPDS [36] is also included for comparison.

(SFE), i.e., high SFE metals have low activation volume, and therefore, higher strain rate sensitivity and vice versa [49]. For low SFE metals, such as Cu (SFE = 45 mJ/m^2 [43]), plastic response and crack growth behavior do not significantly differ between conventional and ultrasonic frequencies [13]. The SFE of γ phases in Ni-base superalloys, due to the presence of multiple alloying elements, is even lower, ~ 20 to 50 mJ/m^2 [51–54]. Consequently, fatigue resistance of IN718 is not expected to be

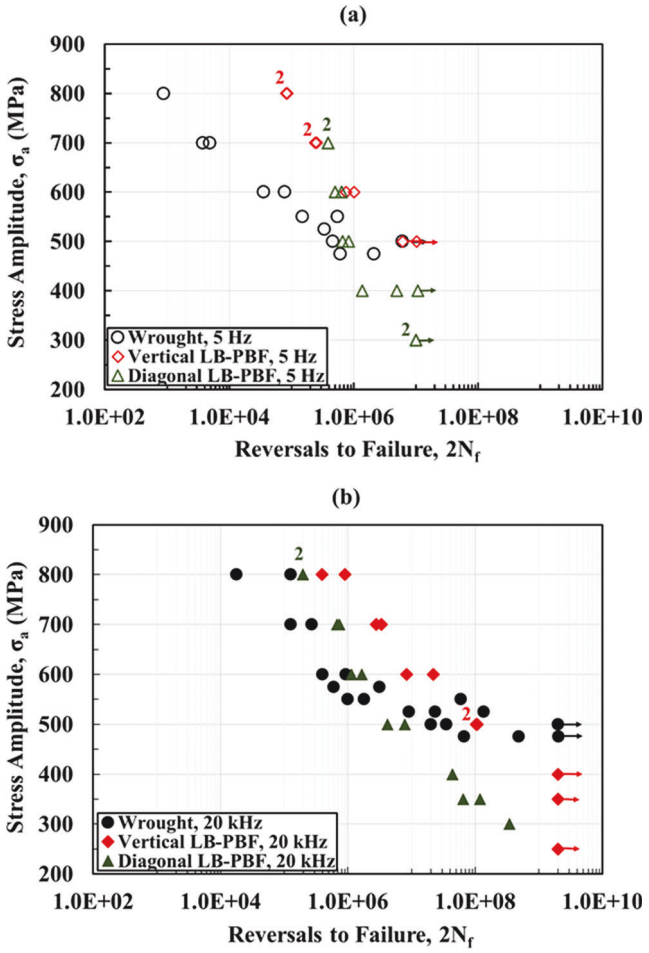

Fig. 8. Fatigue behavior of wrought, vertical LB-PBF, and diagonal LB-PBF IN718 specimens in machined surface condition tested using (a) conventional and (b) ultrasonic fatigue test methods.

much sensitive to the cyclic strain rate.

This rationale, however, contrasts with the data presented in Fig. 6, which indicates an improvement in fatigue life of roughly an order of magnitude for almost all specimens tested under ultrasonic frequency. The discrepancy in fatigue lives between the two testing conditions, may arise from the different ways in which the nominal stress amplitudes are calculated. On one hand, the conventional fatigue tests are force-controlled and force is calculated based on the engineering stress for the targeted stress amplitude. On the other hand, in the resonance based ultrasonic fatigue tests, the stresses are calculated based on the linear elastic modal analysis, which does not account for plastic and anelastic [55] energy dissipation, which may lead to the overestimation of stresses. Therefore, at lower stresses and for less ductile behaving materials, more accurate stresses can be calculated from the elastic modal analysis.

The discrepancy in stress values is reflected in the fracture surfaces of the specimens (see Figs. 9, 10, and 11). It appears that the final fracture regions of the conventionally tested specimens are consistently larger than the ones under ultrasonic tests. Since no ultrasonic tests were run to final fracture (they were terminated when a shift in the resonance frequency of 500 Hz was detected and the specimens pulled apart manually), one can conclude that a higher stress amplitude was experienced in the conventional fatigue tests than in the ultrasonic tests.

To account for this stress discrepancy, a linear elastic fracture mechanics (LEFM) based stress correction is applied to the stress-life data obtained from ultrasonic fatigue tests. The correction assumes that "fracture" occurs at the termination of ultrasonic tests, uses the stresses

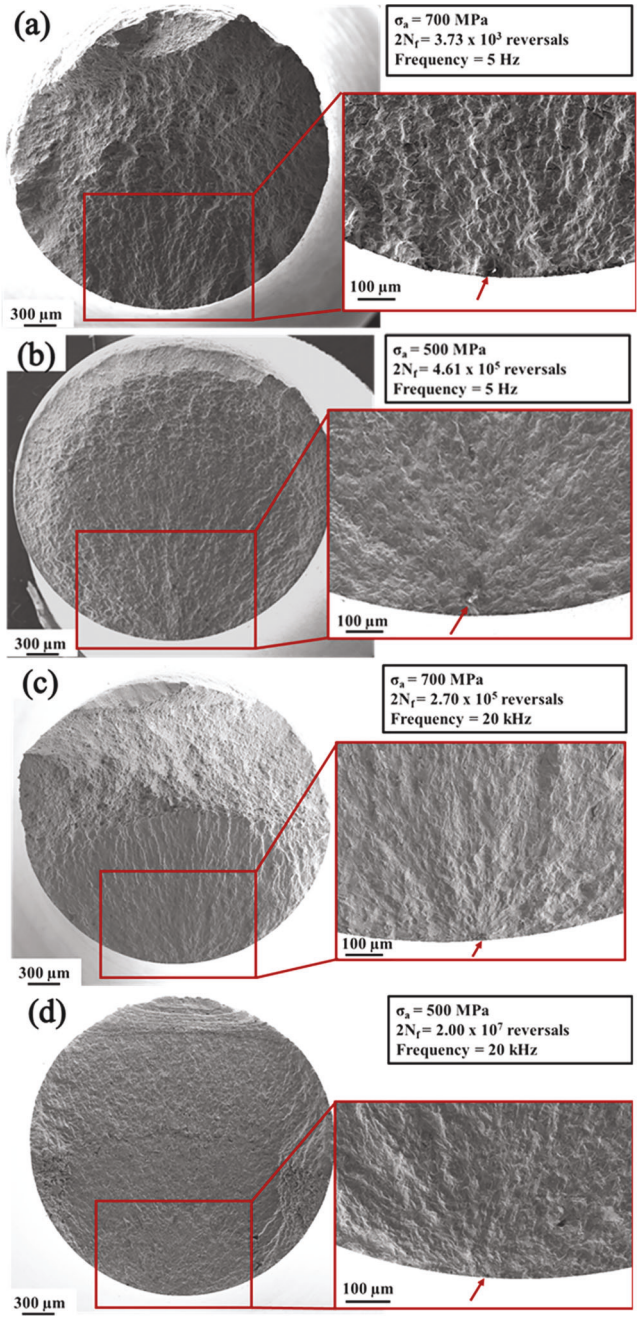

Fig. 9. Representative fracture surfaces of wrought IN718 samples tested under both conventional and ultrasonic loading conditions. The specimens in (a) and (b) were tested at a frequency of 5 Hz. The specimens in (c) and (d) were tested at a frequency of at a frequency of 20 kHz.

and fracture surfaces of the conventional tests as references, and corrects the stresses in ultrasonic fatigue tests based on their fracture surfaces. Specifically, the final crack size (a) before "fracture" for both loading types are compared and at fracture. Considering K_c as the Mode I fracture toughness of the material:

$$K_c = Y\sigma_{max}\sqrt{\pi a} \tag{3}$$

where Y is the geometry factor, and σ_{max} is the remotely applied stress, which equals the stress amplitude in fully reversed cyclic loading.

Assuming that K_c is rate-independent, the corrected stress (σ_{UF}^{C}) in the ultrasonic fatigue tests can be obtained by:

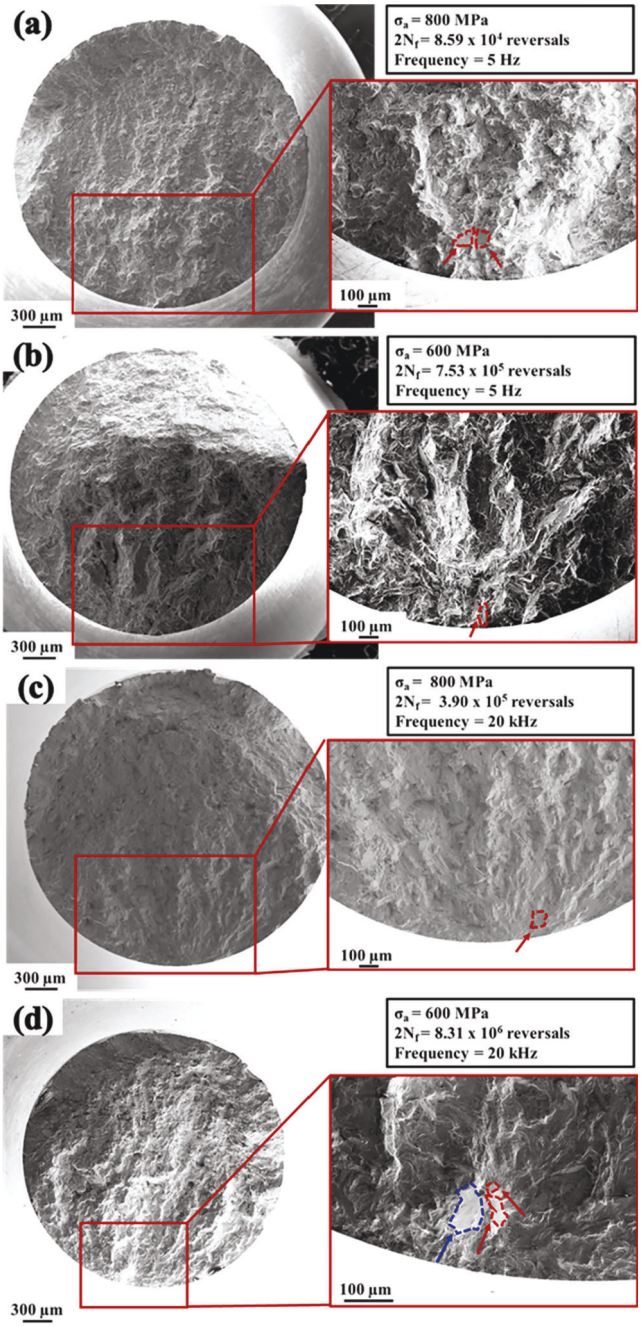

Fig. 10. Representative fracture surfaces of vertical LB-PBF IN718 samples tested under both conventional and ultrasonic loading conditions. The specimens in (a) and (b) were tested at a frequency of 5 Hz. The specimens in (c) and (d) were tested at a frequency of 20 kHz.

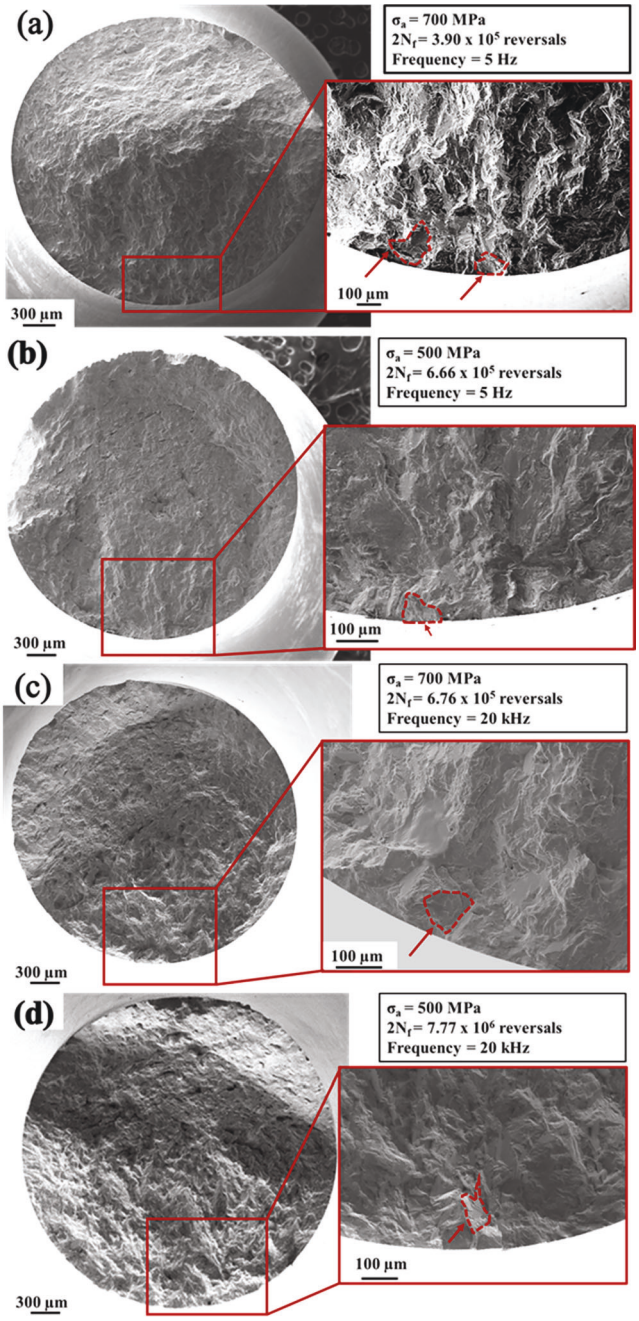

Fig. 11. Representative fracture surfaces of diagonal LB-PBF IN718 samples tested under both conventional and ultrasonic loading conditions. The specimens in (a) and (b) were tested at a frequency of 5 Hz. The specimens in (c) and (d) were tested at a frequency of 20 kHz.

$$\sigma_{UF}^{C} = \sqrt{\frac{a_{CF}}{a_{UF}}} * \sigma_{UF} \tag{4}$$

where a_{CF} and a_{UF} are the effective final crack sizes for specimens under conventional and ultrasonic tests, respectively (see Fig. 12), and σ_{UF} is the intended stress amplitude in the input of "SuperSonic" software for ultrasonic testing. The ratio $\sqrt{\frac{a_{CF}}{a_{UF}}}$ is obtained by analyzing the fracture surfaces of the wrought IN718 specimens failed at 700 MPa (shown in Fig. 12) and 500 MPa stress amplitudes for both conventional and ultrasonic testing. For each stress amplitude, the effective crack lengths, a_{CF} and a_{UF}, are obtained by equating the crack areas on the fracture surfaces (such as the ones indicated by red dashed lines in Fig. 12) to the ideal crack shapes (such as the ones indicated by the blue dash-dot-dot lines in Fig. 12) reported by Thompson and Shepard [56] using finite element analysis. Conversion to ideal crack shapes allows for a relatively objective comparison of crack sizes, even though their shape might not be similar due to microstructural variations. At both stress levels, the ratio $\sqrt{\frac{a_{CF}}{a_{UF}}}$ was calculated to be consistently around 0.85.

The stress-life data from conventional tests, as well as the corrected ones from the ultrasonic tests based on the calculated ratio of 0.85, are presented in Fig. 13. As shown, this stress correction factor appears to have unified the stress-life data from both test frequencies for all specimens; Fig. 13 (a), (b), and (c), respectively, for wrought, V LB-PBF and D LB-PBF IN718. Interestingly, the correlation is also acceptable for the

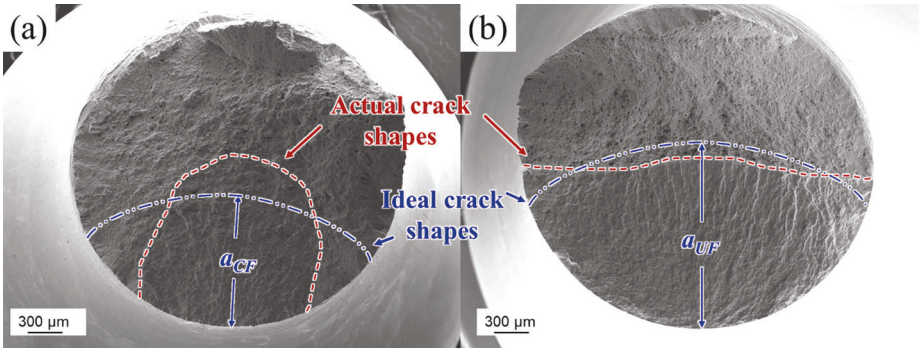

Fig. 12. Typical crack propagation region for wrought IN718 specimens subjected to (a) conventional and (b) ultrasonic testing at 700 MPa stress amplitude.

superimposed stress-life fatigue data of wrought IN718 from MMPDS [35] in Fig. 13 (a). It should be emphasized that the employed Eq. (3) is just to test the suggested hypothesis that the actual stress experienced at the gage section of ultrasonic fatigue specimens might differ from the one calculated based on the elastic modal analysis.

4.2. Effects of material processing on the fatigue behavior

The corrected stress-life behaviors of the IN718 specimens obtained from ultrasonic fatigue tests was shown in Section 4.1 to converge to those from conventional fatigue tests fairly well. As such, the discussion in this section is limited to the observations made in Fig. 8 (a). In summary, V LB-PBF specimens were shown to exhibit better fatigue resistance as compared to D LB-PBF specimens in lower stress levels. This advantage, however, appears to vanish at higher stress levels. In addition, the fatigue resistance of the D LB-PBF specimens appears to be superior to the wrought ones at all stress levels.

The difference in fatigue performance between the LB-PBF and wrought specimens appear to primarily originate from their difference in strength. A secondary reason may be their different crack initiation mechanisms, i.e., PSBs initiation for LB-PBF specimens vs second phase particle initiation for wrought specimens. The heat treatment schedule adopted in the present study has a very limited solutioning time (10 min) at a relatively low temperature (954 °C), which was insufficient to homogenize the micro-segregation of the alloying elements, especially Nb, at the inter-dendritic regions. Indeed, the dendritic microstructure of the LB-PBF specimens fabricated in this study is similar to that of the directly aged LB-PBF IN718 obtained by Gallmeyer et al. [57], where the material achieved a yield strength of 1300 MPa due to the presence of dislocation cell structures stabilized by segregated Nb at the interdimeric regions. The intra-granular misorientations manifested as subgrain low angle boundaries (shown in Fig. 5) may also have provided additional strengthening. The difference in the strength of materials between wrought and LB-PBF IN718 is also demonstrated by the difference in their hardness. Micro-hardness of LB-PBF (465 HV with a standard deviation of 2) was almost two times the micro-hardness of wrought IN718 (151HV with a standard deviation of 80) in this study.

Therefore, at the stress amplitude of 800 MPa, the wrought specimen exhibited significant hysteresis (see Fig. 14) and failed at low cycle regime (below 1000 reversals). On the other hand, the V LB-PBF specimens, due to their substantially higher strength, experienced limited cyclic plasticity, and failed in mid-high cycle regime (~80,000 reversals). The influence of strength attenuated at lower stress levels, as the macroscopic plastic deformation in wrought specimens gradually transitioned to localized slip.

At low stress levels, the crack initiation and propagation of microstructurally small cracks, which can be strongly inhibited by smaller grains, dominates the fatigue life [37]. The wrought specimens have noticeably smaller grains than the LB-PBF ones. Therefore their disadvantage in fatigue performance due to lower strengths and second phase particle induced crack initiation is compensated. Indeed, the fatigue life of the wrought specimens is similar to that of the D LB-PBF specimens at lower stress amplitudes, such as 500 MPa.

The difference in the stress-life behaviors of V and D LB-PBF specimens can be ascribed to the columnar shape of the grains as well as the difference in their orientations. As shown in Figs. 9, 10, and 11 and described in Section 3.3, the initiation sites of fatigue cracks in the LB-PBF and some wrought specimens are identified as facets oriented approximately 45° off the loading axis. These facets are due to planar or near-planar slip bands confined within individual grains. In D LB-PBF specimens, due to its unique orientation of the grains (compare Fig. 4 (a) and 4 (b) for V and D specimens), slip planes of grains elongated at 45° angle with respect to the loading axis can be significantly greater than the ones in V LB-PBF specimens, in which grains are elongated parallel to the loading axis.

CISs and microstructure of wrought, V, and D LB-PBF specimens are visually compared in Fig. 15. The corresponding statistics of CIS size (projected in the loading plane) in different specimens have been provided in Table 4. Note that the facet marked by blue dashed line in Fig. 10 (d) does not form ~45° angle with the loading axis. Instead, it is nearly perpendicular to the loading axis, and therefore, is not included (this is the only specimen excluded in the calculation of CISs) in Table 4.

Indeed, as shown in Figs. 10, 11, and 15 and as summarized in Table 4, the average size of the projected CISs in the D LB-PBF specimens is significantly larger than in the one calculated for the V LB-PBF specimens, which explains the significantly shorter fatigue lives of D LB-PBF specimens at lower stress amplitudes (e.g., at 500 MPa), where the initiation stage dominates the fatigue life. At higher stress levels (such as 700 MPa stress amplitude), the fatigue life is dominated by the growth of the fatigue cracks, which has been shown to be quite insensitive to the build orientation [58]; thus, the benefit of the V LB-PBF specimens due to the orientations of the grains vanishes.

The results presented in this study highlight the strong influence of microstructure on the initiation as well as the early propagation of fatigue cracks. As shown in Fig. 15, the regions near the CISs appears to be faceted, with clear striations on the surfaces of the wrought specimens, whose size and morphology correlate well with the grains in the respective material. Finally, the same trend persists in both sets of specimens tested under conventional and ultrasonic frequencies, as evident in Fig. 15.

4.3. Effects of defects in the initiation of fatigue cracks

Although the fatigue cracks in wrought specimens initiated from an assortment of sources, including manufacturing defects, including carbides and Laves phases, as well as the PSBs in grains, almost all the fatigue failure of LB-PBF specimens initiated from PSBs within grains under both frequency conditions (see Figs. 10 and 11); only two CISs were near pores (see Figs. 10 (d) and 11 (d)), although the evidence of these pores serving as the crack initiating defects is not strong. This

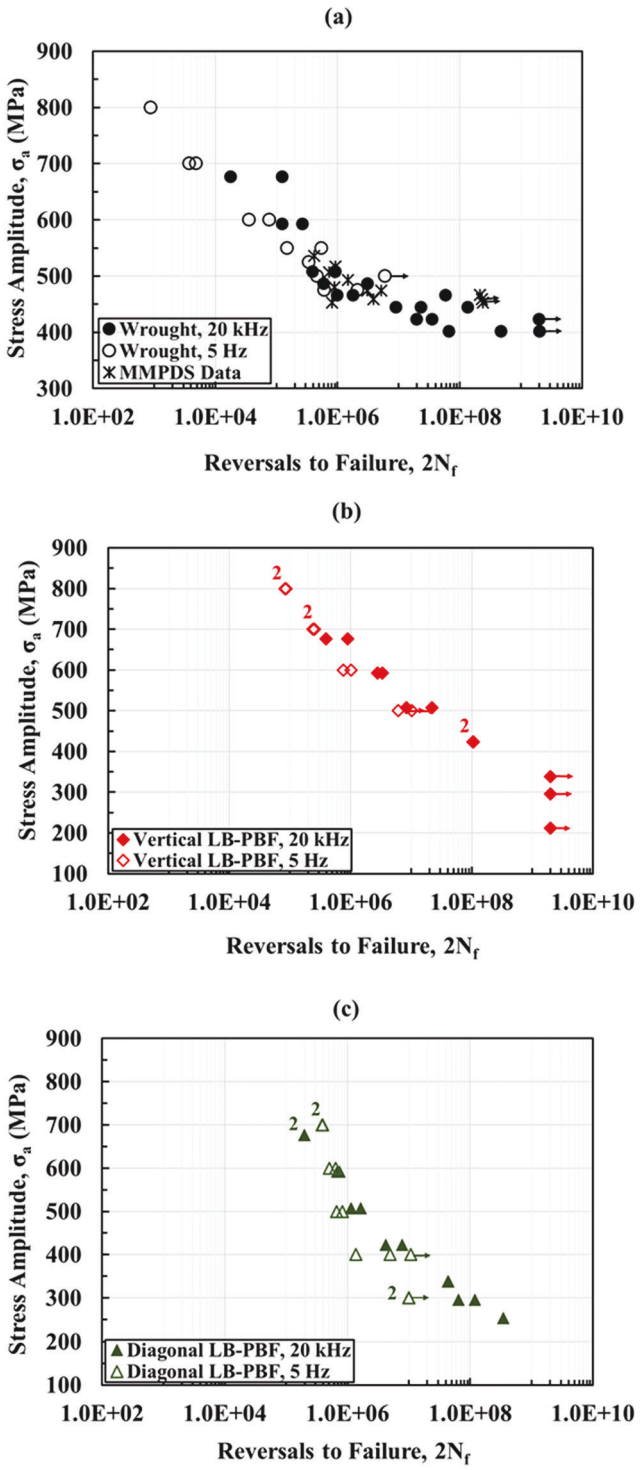

Fig. 13. Fatigue behavior after stress correction of ultrasonic specimens for (a) wrought IN718 specimens, (b) vertical LB-PBF, and (c) diagonal LB-PBF IN718 specimens; tested using both conventional and ultrasonic fatigue test methods. In (a), wrought data from this study was also compared with stress-life data of wrought IN718 data obtained from MMPDS [36].

contrasts with the observations in the literature that the volumetric defects are typically responsible for the crack initiating in machined laser beam-directed energy deposition (LB-DED) and LB-PBF Ni-base superalloys under conventional [59] and ultrasonic [19] fatigue tests, respectively. The discrepancy between the literature and this study in this regard can be attributed to 1) the hour-glass geometry of the specimens, 2) the lower defect content, and 3) the relatively large columnar

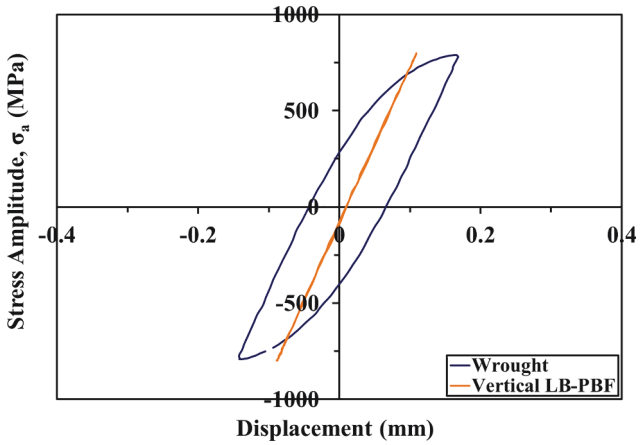

Fig. 14. Comparison of hysteresis loops of wrought and vertical LB-PBF IN718 specimens, tested at 800 MPa stress amplitude.

grains observed in the LB-PBF specimens in the present work.

The conventional fatigue tests on round IN718 specimens with straight gage section fabricated using LB-DED AM system by Johnson et al. [59] revealed the initiation of fatigue cracks from intermetallic particles and pores. Due to the use of specimens with straight gage sections, a much larger material volume, and therefore, a much larger population of defects, was subjected to a uniformly applied maximum stress, which significantly increases the likelihood of crack initiation from these defects due to the associated stress concentrations. The ultrasonic fatigue tests by Yang et al. [19] used a specimen geometry similar to the one used in this study (see Fig. 1 (d)), which limits the maximum stress to the thinnest cross-section at the gage. The defect-initiated cracks reported by Yang et al. [19] may indicate a significantly higher population of large defects in their specimens than the IN718 specimens fabricated in the present study. For instance, they reported crack initiation from lack-of-fusion defects [19], which were absent from the specimens fabricated in the present work (see Fig. 2).

Indeed, the only volumetric defect type identified in the LB-PBF specimens by the X-ray CT in this study has been gas-entrapped pores with most of them within the size range of 5–15 μm. Although the largest defect identified has a diameter > 40 μm, its population is extremely low — only one in the 25.9 mm^3 volume scanned. Therefore, the probability of it residing on the maximum-stress cross-section of the hour-glass shaped specimens is very low. This is schematically illustrated in Fig. 16 (a). This is an indication that the population of the large defects in the present work is significantly lower than reported in [19].

A schematic illustration of potential positions of slip bands relative to a pore are shown in Fig. 16. Although the smaller pores in the LB-PBF specimens in this work may promote the formation of PSB in their vicinity (see the red band illustrated in Fig. 16 (b)), the probability of such pores potentially occurring on a long PSB is generally low, due to the random nature of the pore distribution. As a result, short PSBs may be arrested easily at grain boundaries, while longer PSBs elsewhere (depicted as blue ones in Fig. 16 (b)) may propagate through grain boundaries (indicated by blue dashed arrows) and/or develop into small cracks easier. As the cyclic fatigue behavior of IN718 does not exhibit apparent cyclic strain rate sensitivity, the competing roles of the volumetric defects and long slip distances within the columnar grains in LB-PBF IN718 discussed here should equally apply to both conventional and ultrasonic fatigue tests.

Although the existence of such a competition is intuitive, determining the exact conditions (e.g., defect size and type, grain size, and texture) in which one dominates the other require a precise control of the microscopic characteristics of the material that may be proven infeasible experimentally. To this end, a parametric study of the synergistic effects of volumetric defects and the surrounding microstructure

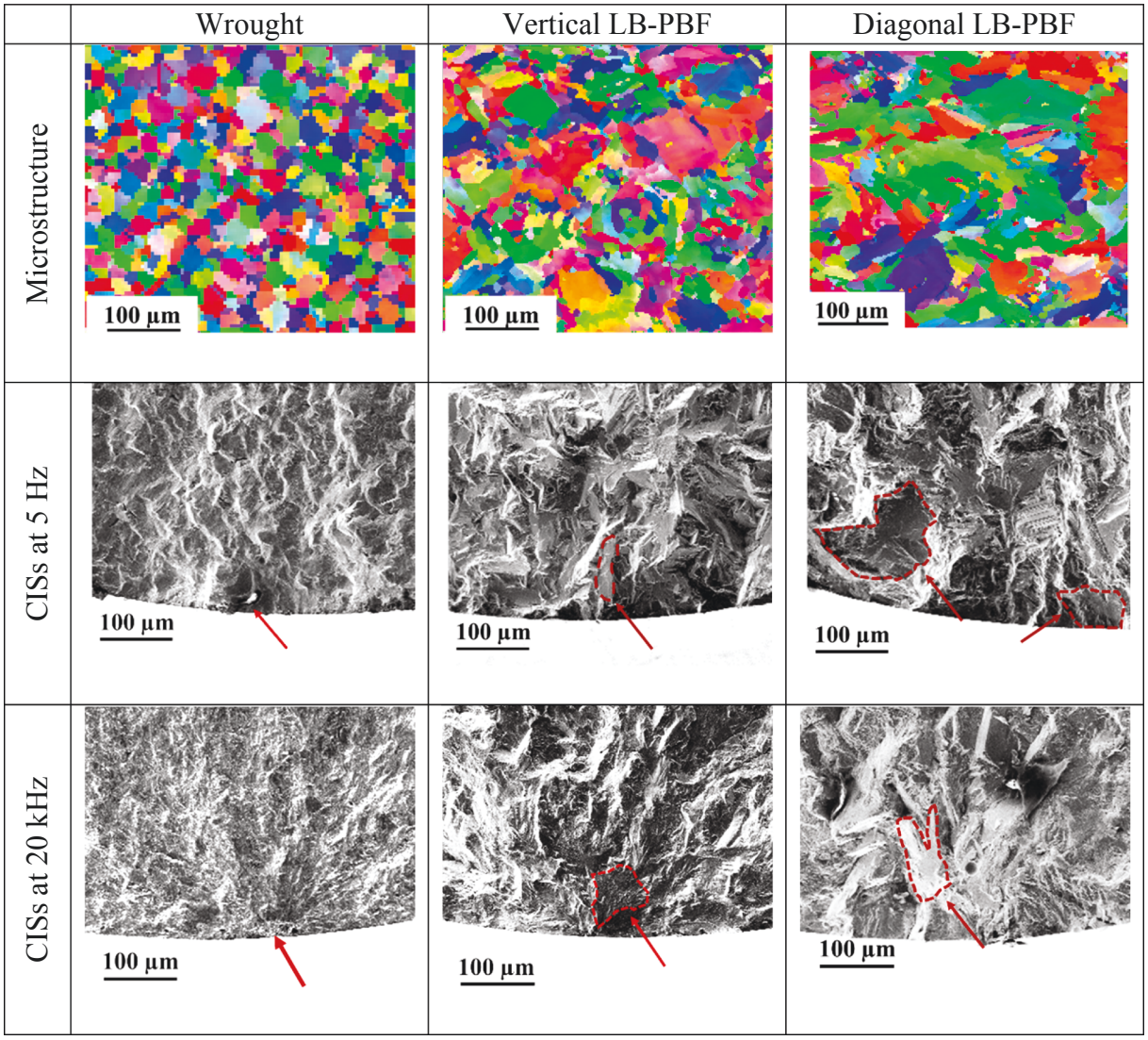

Fig. 15. Comparison of microstructure and fracture surfaces among wrought, vertical LB-PBF, and diagonal LB-PBF IN718 specimens.

Table 4
Crack initiating size (length) comparisons between vertical LB-PBF and diagonal LB-PBF IN718 specimens.

Frequency	Vertical LB-PBF	Diagonal LB-PBF
5 Hz	79 μm	110 μm
20 kHz	53 μm	94 μm

on the fatigue resistance of LB-PBF IN718 using numerical simulations (such as the crystal plasticity finite element method) may be needed and will be presented in the following work.

5. Conclusions

In this study, the effects of test frequency and layer orientation on the fatigue resistance in HCF and VHCF regimes of IN718 manufactured via an LB-PBF process were investigated. LB-PBF specimens were fabricated and subjected to post-process heat treatment identical to that of the as-received wrought material. The effect of layer orientation on the fatigue resistance of the LB-PBF IN718 was investigated by fabricating specimens vertically and diagonally with respect to the build platform. Comparing data obtained from both conventional and ultrasonic fatigue tests on specimens with similar geometries, the effect of testing frequency (i.e., cyclic strain rate) was also evaluated. This study demonstrated that the apparent effects of test frequencies obtained from a direct comparison of conventional and ultrasonic fatigue tests may be influenced by other factors. Equivalency between the test methods needs to be carefully established before ultrasonic fatigue testing can be used to expedite the generation of materials data. The following conclusions were drawn from this study:

1. The LB-PBF processed IN718 in this study was found to contain a relatively coarse columnar microstructure (column width > 70 μm) with γ grains perpendicular to the build platform. In addition, the as-solidified dendritic microstructure still persisted after the SAE AMS2774E heat treatment.
2. The volumetric defect type in the LB-PBF specimens was identified to be gas-entrapped pores, mostly with a nominal size within 5–15 μm. These pores were found to reside reasonably well within the coarse columnar grains.
3. Fractography analysis revealed that specimens subjected to ultrasonic fatigue tests experienced stress amplitudes lower than the prescribed nominal values. Correcting the stresses in the ultrasonic fatigue tests, the stress-life behaviors observed in both testing methods/frequencies appeared consistent. Accordingly, no significant frequency effect was observed.

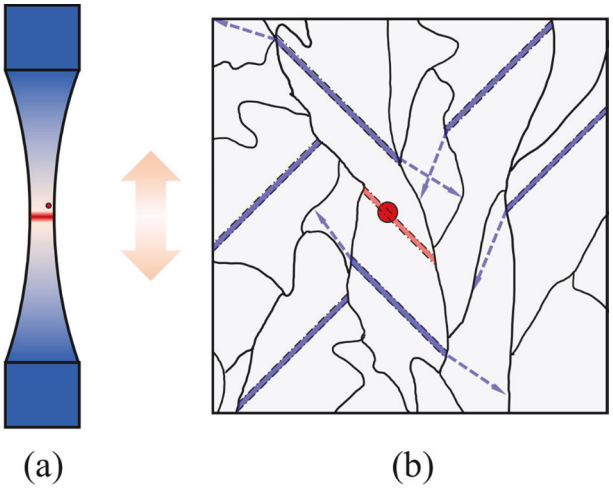

Fig. 16. Schematic illustrations of (a) the relative position of a large volumetric defect and the maximum loading plane in hour-glass shaped specimens and (b) a slip band (red band) initiated by a small defect (red circle) compared to other, potentially longer slip bands (blue bands). (For interpretation of the references to colour in this figure legend, the reader is referred to the web version of this article.)

4. In general, the LB-PBF specimens happened to exhibit a better fatigue resistance than wrought at higher stress amplitudes under both loading frequencies, which attenuated at lower stress amplitudes. The vertical LB-PBF specimens were found to be more fatigue resistant than the diagonal LB-PBF ones, with the exception of cases at higher stress amplitudes.
5. Fatigue cracks of the LB-PBF specimens were seen to almost always initiate from PSBs instead of from volumetric defects. This is in part due to the low probability of a large volumetric defect appearing on the maximum stress planes of hour-glass specimens. In addition, this could also be due to the vanishingly small likelihood of a defect residing on a large PSB favorable for crack initiation.

One overall learning from this study is related to the use of hour-glass specimens to generate mechanical properties for AM materials. Due to the very small volume of the material experiencing the maximum stress at the gage of these specimens, the full effect of volumetric defects may not be accounted for. Therefore, the data generated from specimens with straight gage section may be more appropriate as the effect of volumetric defects on fatigue behavior can be captured more effectively.

Disclaimer

This report was prepared as an account of work sponsored by an agency of the United States Government. Neither the United States Government nor any agency thereof, nor any of their employees, makes any warranty, express or implied, or assumes any legal liability or responsibility for the accuracy, completeness, or usefulness of any information, apparatus, product, or process disclosed, or represents that its use would not infringe privately owned rights. Reference herein to any specific commercial product, process, or service by trade name, trademark, manufacturer, or otherwise does not necessarily constitute or imply its endorsement, recommendation, or favoring by the United States Government or any agency thereof. The views and opinions of authors expressed herein do not necessarily state or reflect those of the United States Government or any agency FA R&D Special TC NOVEMBER 2017- FF Page 4 of 12 thereof.

Declaration of Competing Interest

The authors declare that they have no known competing financial interests or personal relationships that could have appeared to influence the work reported in this paper.

Acknowledgments

This material is based upon work partially supported by the National Aeronautics and Space Administration (NASA) through the University of Central Florida's NASA Florida Space Grant Consortium. The involvement of Auburn University's NCAME in this project is partially supported by NASA Award Nos. NNX17AJ93A and 80MSFC17M0023 and the U.S. Department of Energy, Office of Science, Office of Basic Energy Sciences, under Award Number DE-SC0019378. Anton Paar GmbH is also acknowledged for providing the Nano-Indentation Hardness Testing (NHT2) instrument for this study.

References

[1] Du D, Dong A, Shu D, Zhu G, Sun B, Li X, et al. Influence of build orientation on microstructure, mechanical and corrosion behavior of Inconel 718 processed by selective laser melting. Mater. Sci. Eng. A. 2019;760:469–80.
[2] Mostafa A, Picazo Rubio I, Brailovski V, Jahazi M, Medraj M. Structure, texture and phases in 3D printed IN718 alloy subjected to homogenization and HIP treatments. Metals (Basel) 2017;7:196.
[3] Zhang D, Niu W, Cao X, Liu Z. Effect of standard heat treatment on the microstructure and mechanical properties of selective laser melting manufactured Inconel 718 superalloy. Mater. Sci. Eng. A. 2015;644:32–40.
[4] Wycisk E, Siddique S, Herzog D, Walther F, Emmelmann C. Fatigue performance of laser additive manufactured Ti–6Al–4V in very high cycle fatigue regime up to 109 cycles. Front. Mater. 2015;2.
[5] Wycisk E, Solbach A, Siddique S, Herzog D, Walther F, Emmelmann C. Effects of Defects in Laser Additive Manufactured Ti-6Al-4V on Fatigue Properties. Phys. Procedia. 2014;56:371–8.
[6] R. Russell, D. Wells, J. Waller, B. Poorganji, E. Ott, T. Nakagawa, H. Sandoval, N. Shamsaei, M. Seifi, Qualification and certification of metal additive manufactured hardware for aerospace applications, in: Addit. Manuf. Aerosp. Ind. (2019) 33–66.
[7] Texier D, Cormier J, Villechaise P, Stinville J-C, Torbet CJ, Pierret S, et al. Crack initiation sensitivity of wrought direct aged alloy 718 in the very high cycle fatigue regime: the role of non-metallic inclusions. Mater. Sci. Eng. A. 2016;678:122–36.
[8] Solberg K, Torgersen J, Berto F. Fatigue Behaviour of Additively Manufactured Inconel 718 Produced by Selective Laser Melting. Procedia Struct. Integr. 2018:1762–7.
[9] Stöcker C, Zimmermann M, Christ HJ. Effect of precipitation condition, prestrain and temperature on the fatigue behaviour of wrought nickel-based superalloys in the VHCF range. Acta Mater 2011.
[10] Siddique S, Imran M, Wycisk E, Emmelmann C, Walther F. Fatigue Assessment of Laser Additive Manufactured AlSi12 Eutectic Alloy in the Very High Cycle Fatigue (VHCF) Range up to 1E9 cycles. Mater. Today Proc. 2016;3:2853–60.
[11] Berger C, Kaiser B. Results of very high cycle fatigue tests on helical compression springs. Int. J. Fatigue. 2006;28:1658–63.
[12] Eric W, Claus E, Shafaqat S, Frank W. High cycle fatigue (HCF) performance of Ti-6Al-4V alloy processed by selective laser melting. Adv. Mater. Res. 2013;816–817:134–9.
[13] Mayer H. Fatigue crack growth and threshold measurements at very high frequencies. Int. Mater. Rev.; 1999.
[14] Zhang Y, Duan Z, Shi H. Comparison of the very high cycle fatigue behaviors of INCONEL 718 with different loading frequencies. Sci. China Physics, Mech. Astron. 2013;56:617–23.
[15] Chen Q, Kawagoishik N, Wang Q, Yan N, Ono T, Hashiguchi G. Small crack behavior and fracture of nickel-based superalloy under ultrasonic fatigue. Int. J. Fatigue. 2005;27:1227–32.
[16] Belan J. High frequency fatigue test of in 718 alloy – microstructure and fractography evaluation. Metalurgija. 2015;54:59–62.
[17] Amanov A, Pyun YS, Kim JH, Suh CM, Cho IS, Kim HD, et al. Ultrasonic fatigue performance of high temperature structural material Inconel 718 alloys at high temperature after UNSM treatment. Fatigue Fract. Eng. Mater. Struct. 2015;38:1266–73.
[18] Bathias C. Fatigue Limit in Metals. Hoboken, USA: John Wiley & Sons Inc; 2013.
[19] Yang K, Huang Q, Wang Q, Chen Q. Competing crack initiation behaviors of a laser additively manufactured nickel-based superalloy in high and very high cycle fatigue regimes. Int. J. Fatigue. 2020;136:105580.
[20] Ma X, Duan Z, Shi H, Murai R, Yanagisawa E. Fatigue and fracture behavior of nickel-based superalloy Inconel 718 up to the very high cycle regime. J. Zhejiang Univ. A. 2010;11:727–37.
[21] Kawagoishi C. Nisitani, Fatigue strength of Inconel 718 at elevated temperatures. Fatigue & Fract. Eng. Mater. Struct. 2000;23:209–16.
[22] G.E. Korth, G.R. Smolik, Status report of physical and mechanical test data of Alloy 718 (Technical Report) | OSTI.GOV.
[23] Yadollahi A, Shamsaei N. Additive manufacturing of fatigue resistant materials: Challenges and opportunities. Int. J. Fatigue. 2017;98:14–31.

[24] Shrestha R, Simsiriwong J, Shamsaei N. Fatigue behavior of additive manufactured 316L stainless steel parts: Effects of layer orientation and surface roughness. Addit. Manuf. 2019;28:23–38.
[25] Fatemi A, Molaei R, Simsiriwong J, Sanaei N, Pegues J, Torries B, et al. Fatigue behaviour of additive manufactured materials: An overview of some recent experimental studies on Ti-6Al-4V considering various processing and loading direction effects. Fatigue Fract. Eng. Mater. Struct. 2019;42:991–1009.
[26] Molaei R, Fatemi A, Sanaei N, Pegues J, Shamsaei N, Shao S, et al. Fatigue of additive manufactured Ti-6Al-4V, Part II: The relationship between microstructure, material cyclic properties, and component performance. Int. J. Fatigue. 2020;132:105363.
[27] Nayeb-Hashemi H. Failure modes of specimens containing surface flaws under cyclic torsion. Exp. Mech. 1987;27:51–6.
[28] Yadollahi A, Shamsaei N, Thompson SM, Elwany A, Bian L. Effects of building orientation and heat treatment on fatigue behavior of selective laser melted 17–4 PH stainless steel. Int. J. Fatigue. 2017;94:218–35.
[29] AMS2774E Heat Treatment Wrought Nickel Alloy and Cobalt Parts, SAE Int. (2016).
[30] Ultrasonic Fatigue Testing System | Shimadzu USF-2000A.
[31] E466-15, Practice for conducting force controlled constant amplitude axial fatigue tests of metallic materials, ASTM B. Stand. (2015).
[32] Nunes RM, Pereira D, Clarke T, Hirsch TK. Delta Phase Characterization in Inconel 718 Alloys Through X-ray Diffraction. ISIJ Int. 2015;55:2450–4.
[33] Nezhadfar PD, Johnson AS, Shamsaei N. Fatigue behavior and microstructural evolution of additively manufactured Inconel 718 under cyclic loading at elevated temperature. Int. J. Fatigue. 2020;136:105598.
[34] Hall RC. The Metallurgy of Alloy 718. J. Basic Eng. 1967;89:511–6.
[35] R.C. Rice, J.L. Jackson, J. Bakuckas, S. Thompson, Metallic Materials Properties Development and Standardization (MMPDS). National Technical Reports Library - NTIS, (2003) 1728.
[36] H. Mughrabi, R. Wang, K. Differt, U. Essmann, Fatigue Crack Initiation by Cyclic Slip Irreversibilities in High-Cycle Fatigue, in: Fatigue Mech. Adv. Quant. Meas. Phys. Damage, ASTM International, 100 Barr Harbor Drive, PO Box C700, West Conshohocken, PA 19428-2959, 1983: pp. 5-5–41.
[37] Stephens RI, Fatemi A, Stephens RR, Fuchs HO. Metal Fatigue in Engineering. 2nd Edition. Comput: Eng; 2000.
[38] Mahanta B, Tripathy A, Vishal V, Singh TN, Ranjith PG. Effects of strain rate on fracture toughness and energy release rate of gas shales. Eng. Geol. 2017;218:39–49.
[39] Ural A, Zioupos P, Buchanan D, Vashishth D. The effect of strain rate on fracture toughness of human cortical bone: A finite element study. J. Mech. Behav. Biomed. Mater. 2011;4:1021–32.
[40] Wan H-Y, Zhou Z-J, Li C-P, Chen G-F, Zhang G-P. Enhancing Fatigue Strength of Selective Laser Melting-Fabricated Inconel 718 by Tailoring Heat Treatment Route. Adv. Eng. Mater. 2018;20:1800307.
[41] Sangid MD. The physics of fatigue crack initiation. Int. J. Fatigue. 2013;57:58–72.
[42] Ling L-S-B, Yin Z, Hu Z, Wang J, Sun B-D. Effects of the γ″-Ni3Nb Phase on Fatigue Behavior of Nickel-Based 718 Superalloys with Different Heat Treatments. Materials (Basel). 2019;12:3979.
[43] Hirth JP, Lothe J, Mura T. Theory of Dislocations. J. Appl. Mech. 1983;50:476–7.
[44] Li W, Li S, Liu J, Zhang A, Zhou Y, Wei Q, et al. Effect of heat treatment on AlSi10Mg alloy fabricated by selective laser melting: Microstructure evolution, mechanical properties and fracture mechanism. Mater. Sci. Eng. A. 2016;663:116–25.
[45] Shao S, Khonsari MM, Guo S, Meng WJ, Li N. Overview: Additive Manufacturing Enabled Accelerated Design of Ni-based Alloys for Improved Fatigue Life. Addit. Manuf. 2019;29:100779.
[46] Lothe J, Hirth JP. Dislocation Climb Forces. J. Appl. Phys. 1967;38:845–8.
[47] Dodaran M, Khonsari MM, Shao S. Critical operating stress of persistent slip bands in Cu. Comput. Mater. Sci. 2019;165:114–20.
[48] Zhang JY, Liu G, Sun J. Strain rate effects on the mechanical response in multi- and single-crystalline Cu micropillars: Grain boundary effects. Int. J. Plast. 2013;50:1–17.
[49] Wei Q. Strain rate effects in the ultrafine grain and nanocrystalline regimes—influence on some constitutive responses. J. Mater. Sci. 2007;42:1709–27.
[50] Kiener D, Fritz R, Alfreider M, Leitner A, Pippan R, Maier-Kiener V. Rate limiting deformation mechanisms of bcc metals in confined volumes. Acta Mater. 2019;166:687–701.
[51] Pettinari F, Douin J, Saada G, Caron P, Coujou A, Clément N. Stacking fault energy in short-range ordered γ-phases of Ni-based superalloys. Mater. Sci. Eng. A. 2002;325:511–9.
[52] Fournier D, Pineau A. Low cycle fatigue behavior of inconel 718 at 298 K and 823 K. Metall. Trans. A. 1977;8:1095–105.
[53] Xu H, Zhang ZJ, Zhang P, Cui CY, Jin T, Zhang ZF. The synchronous improvement of strength and plasticity (SISP) in new Ni-Co based disc superalloys by controling stacking fault energy. Sci. Rep. 2017;7:8046.
[54] You X, Tan Y, Shi S, Yang J-M, Wang Y, Li J, et al. Effect of solution heat treatment on the precipitation behavior and strengthening mechanisms of electron beam smelted Inconel 718 superalloy. Mater. Sci. Eng. A. 2017;689:257–68.
[55] Arechabaleta Z, van Liempt P, Sietsma J. Quantification of dislocation structures from anelastic deformation behaviour. Acta Mater. 2016;115:314–23.
[56] Thompson KD, Sheppard SD. Stress intensity factors in shafts subjected to torsion and axial loading. Eng. Fract. Mech. 1992;42:1019–34.
[57] Gallmeyer TG, Moorthy S, Kappes BB, Mills MJ, Amin-Ahmadi B, Stebner AP. Knowledge of process-structure-property relationships to engineer better heat treatments for laser powder bed fusion additive manufactured Inconel 718. Addit. Manuf. 2020;31:100977.
[58] Sabelkin VP, Cobb GR, Shelton TE, Hartsfield MN, Newell DJ, O'Hara RP, et al. Mitigation of anisotropic fatigue in nickel alloy 718 manufactured via selective laser melting. Mater. Des. 2019;182:108095.
[59] Johnson AS, Shao S, Shamsaei N, Thompson SM, Bian L. Microstructure, Fatigue Behavior, and Failure Mechanisms of Direct Laser-Deposited Inconel 718. JOM. 2017;69:597–603.